Global presence and absence of ultra-low velocity zones as seen by Sdiff postcursors

J. R. Atkins[1], C. Martin[2], S. Cottaar[1]

[1]Bullard Laboratories, Department of Earth Sciences, University of Cambridge, CB3 0EZ, UK
[2]Department of Geosciences, Utrecht University, 3854 CB, Netherlands

Key Points:

- Most of the core-mantle boundary lacks evidence for ultra-low velocity zone presence from $\mathrm{S_{diff}}$
- Ultra-low velocity zones seen with $\mathrm{S_{diff}}$ lie preferentially along large low-velocity province edges and under surface hotspots
- Six ultra-low velocity zones account for 99% of regions of positive detections

---

Corresponding author: James Atkins, `jra64@cam.ac.uk`

Abstract

The core-mantle boundary is a region of significant lateral heterogeneity. Two antipodal large low-velocity provinces (LLVPs) dominate the lower mantle, while smaller but more extreme ultra-low velocity zones (ULVZs) pepper the lowermost mantle in a variety of morphologies. These ULVZs have been linked to both the edges of LLVPs and to plume-related hotspots, the latter of which may plausibly be fed or anchored by ULVZs.

In this study, we produce a global map of ULVZs using the phase S_{diff}, picking over 2 million traces and detecting nearly 100,000 postcursors to S_{diff} and over 900,000 null observations. Nearly all regions of ULVZ presence can be explained by six 'S_{diff}-ULVZs', which are found to preferentially lie both underneath hotspots and near LLVP edges. It is possible that there exist multiple types of ULVZs, and those large-scale ULVZs that S_{diff} are sensitive to appear to be linked to some hotspots and the edges of LLVPs, while others may not be. Notably, we find that the large majority of the core-mantle boundary lacks evidence for the presence of large-scale ULVZs.

Plain Language Summary

Seismologists analyse shear waves that travel along the core-mantle boundary, called S_{diff}, as they are sensitive to structures on the boundary. If the wave interacts with a large structure with extremely reduced seismic velocities, such as an ultra-low velocity zone (ULVZ), it causes an additional arrival at seismic stations which we call $S_{\text{diff}}+$. $S_{\text{diff}}+$ has been detected before in many stations, and seismologists have used it to infer the locations of various large-scale ULVZs that lie on the core-mantle boundary. Here, we use a global data set of S_{diff} to create a map of where ULVZs are present and absent across the core-mantle boundary globally, finding that a majority of the core-mantle boundary lacks large ULVZs. Regions where we detect $S_{\text{diff}}+$ can be explained by just six main ULVZs, which we find lie at the edges of major mantle features called large low-velocity provinces and underneath some major volcanic centres on the Earth's surface. It is plausible that ULVZs at the core-mantle boundary may lie at the base of mantle plumes that feed surface volcanism and may contribute to anomalous geochemical signatures from volcanic rocks found on the surface.

1 Introduction

The lowermost mantle is a highly heterogeneous region that is host to many laterally variable structures that impact mantle dynamics and surface processes. The largest of these are the two antipodal Large Low-Velocity Provinces (LLVPs) below the Pacific and Africa, which together cover approximately 30% of the surface the Core-Mantle Boundary (CMB; McNamara, 2019; Cottaar & Lekic, 2016). Present in global tomographic models, they are thousands of kilometres across and rise hundreds of kilometres into the lower mantle, although their tops are fairly elusive.

Ultra-Low Velocity Zones (ULVZs) are much smaller structures that lay atop the CMB, with extreme reductions of up to 50% (e.g. Rondenay & Fischer, 2003) and 25% (e.g. Brown et al., 2015) in shear and compressional wave velocities, respectively. Their morphology varies greatly (Yu & Garnero, 2018), with lateral sizes varying between tens of kilometres (Rost et al., 2005) to almost 1,000 kilometres across (Cottaar & Romanowicz, 2012; Thorne et al., 2013; Yuan & Romanowicz, 2017). The largest ULVZs — typically considered to be 500 km wide or more — are sometimes called 'mega-ULVZs' (Thorne et al., 2013).

The constitution of ULVZs is poorly constrained, and many hypotheses have been put forward. One possibility is partial melting of ambient mantle (Williams & Garnero,

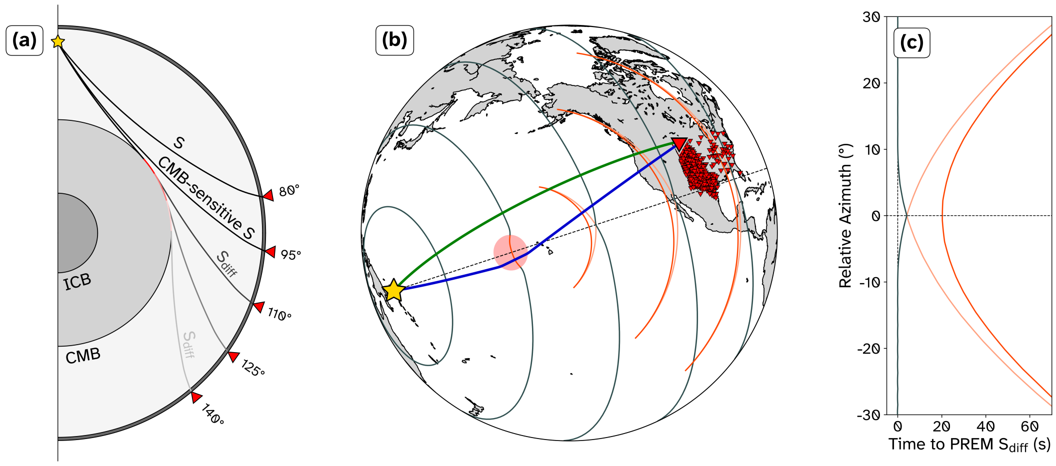

Figure 1. (a) Propagation of S and S_{diff} seismic phases from an earthquake (yellow star) to receivers (red triangles) through a cross-section of the Earth. S_{diff} has a diffracting leg along the CMB (red line), along which it attenuates with distance. (b) Wavefront propagation of S_{diff} from an earthquake (yellow star), calculated using the 2D wavefront tracker (Hauser et al., 2008; Martin et al., 2023b). The wavefront propagates through time (sequential grey lines), producing postcursor signals (orange and light orange) as it passes across a ULVZ (red circle). A receiver (large red triangle) detects the direct arrival (S_{diff}, green line) and an additional delayed arrival due to refraction through the ULVZ (S_{diff}+, blue line) at a different angle to the direct backazimuth. Additional stations (small red triangles) create a record section for this geometry. This geometry relates to the data in Figures 2c and 3a. (c) Variation of S_{diff} (grey) and S_{diff}+ (orange) delay times relative to the S_{diff} arrival time predicted by PREM (Preliminary Reference Earth Model; Dziewonski & Anderson, 1981) with azimuth relative to the source-ULVZ axis. The intermediate arrival in light orange has low amplitude in 3D synthetics and is not observed in data.

1996) or subducted material (Ohtani & Maeda, 2001; J. Liu et al., 2016), although there may be issues in how to keep this melt from draining to a global layer on the CMB (Hernlund & Tackley, 2007; Dannberg et al., 2021). Alternatively they may be solid, in which case heterogeneities would be driven purely by changes in composition. This can be achieved in a number of ways such as iron-enrichment of ferropericlase (Muir & Brodholt, 2016; Dobrosavljevic et al., 2019), subducted materials (Dobson & Brodholt, 2005), or reactions with or sedimentation from the outer core (Buffett et al., 2000; J. Liu et al., 2017). The variety of observed ULVZ characteristics and morphologies mean that a number of possible origin and composition scenarios may plausibly be represented in the lowermost mantle.

ULVZs have been proposed to be geographically correlated with both LLVP edges (e.g. Lai et al., 2022; McNamara et al., 2010) and hotspots (e.g. Helmberger et al., 1998; Wen, 2000; Cottaar et al., 2022). LLVP edges and hotspots have themselves been linked to each other, with LLVP edges suggested to host zones of plume generation that produce areas of widespread surface magmatic activity (Large Igneous Provinces or LIPs; Torsvik et al., 2006; Cucchiaro et al., 2025). In tomographic models, some but not all hotspot plumes are observed to have a continuous conduit of slow velocities down to the CMB (Courtillot et al., 2003; Marignier et al., 2020), often with large horizontal deviations between their surface and CMB positions. Mega-ULVZs have been suggested as reservoirs that contribute to anomalous isotopic or other geochemical signatures in Ocean

Island Basalts fed by deep-rooted plumes (Mundl et al., 2017; Mundl-Petermeier et al., 2020; Cottaar et al., 2022).

Unlike LLVPs, ULVZs are too small and extreme to be imaged directly in current tomographic models, so are only observed in targeted body wave studies. Many seismic phases have been used to detect and model ULVZs, including: phases sensitive to a bounce-point on the CMB such as ScS (Jenkins et al., 2021), ScP (Brown et al., 2015), or PcP (Hutko et al., 2009); core-transiting phases such as SKS and SKKS (Zhang et al., 2009) or PKP (Wen & Helmberger, 1998)); or phases that diffract along the CMB such as S_{diff} (Cottaar & Romanowicz, 2012), $SP_{\text{diff}}KS$ (Thorne et al., 2013), or P_{diff} (Jagt et al., 2024). Bounce-point phases and core-transiting phases are sensitive to the region around their CMB interaction, and can be used to create high resolution 3D maps of ULVZ morphology (Avants et al., 2006; Jenkins et al., 2021; Thorne et al., 2024), but have limited global coverage. In contrast, diffracting phases can achieve global coverage, but have ambiguities in locating and modelling ULVZs at a high resolution.

To date there have been two studies aimed at creating a global map of ULVZs. In order to test the geospatial links to LLVPs and hotspots, Yu and Garnero (2018) compiled individual ULVZ studies published before 2018 into a global map of ULVZ detections, both positive and negative, with combined total CMB coverage of 17.1%. The studies they compiled used a variety of seismic phases which have different sensitivities to each other and may not necessarily be sensitive to the same sorts of structures. Thorne et al. (2021) created a global map of ULVZs using $SP_{\text{diff}}KS$, achieving widespread coverage totalling 56.9% of the CMB. $SP_{\text{diff}}KS$ has inherent ambiguity in locating whether any heterogeneity is located on the source- or receiver-side of the CMB. They conducted an inversion to find the most parsimonious ULVZ distribution, and found that up to 19.7% of the CMB may contain ULVZ-like heterogeneities. However, they only aimed to match anomalous waveforms and disregarded null observations, meaning that the distribution of their raypath coverage has a significant impact on the likelihood of ULVZ presence in any given area.

We present a global map of the presence and absence of ULVZs visible with S_{diff}, hereafter called S_{diff}-ULVZs, using a dataset of 2 million handpicked traces. We locate six S_{diff}-ULVZs which can explain 99% of the regions of S_{diff}-ULVZ presence using a location-finding algorithm, the positions of which are consistent with previously-observed S_{diff}-ULVZs. We also find evidence for unreported areas of S_{diff}-ULVZ presence. After performing statistical analyses to test potential geographical correlations between S_{diff}-ULVZs with both LLVP edges and hotspots, we find that they are correlated with both.

2 Methods

2.1 $S_{\text{diff}}+$

S_{diff} has the potential for complete CMB coverage due to its long diffracting leg, and has been used in many studies before to image ULVZs (e.g. Cottaar & Romanowicz, 2012; Kim et al., 2020; Wolf & Long, 2023). ULVZs are observed in S_{diff} studies in the form of postcursors, hereafter $S_{\text{diff}}+$; out-of-plane energy is refracted through the ULVZ and the resulting additional arrival is $S_{\text{diff}}+$ (Figure 1b). When traces are arranged by azimuth, this additional arrival has an approximately hyperbolic moveout relative to the arrival time of S_{diff} (Figure 1c). The minimum arrival time of this hyperbola is found at the azimuth along which the ULVZ lies relative to the source. $S_{\text{diff}}+$ is sensitive to overall ULVZ volume and velocity reduction, and — to a lesser extent — height via using different frequency bands (e.g. Martin et al., 2024). The long diffracted portion and relatively long period character (typically 10–20 s) of S_{diff} mean that small-scale features — including small or ridge-like ULVZs — may be impossible to resolve. Our map will not show all ULVZs globally, but will show where ULVZs visible with $\mathrm{S_{diff}}$ are or are not present globally.

2.2 Data

We searched for all events between 1995 and 2024 with magnitudes 5.7 or above at all depths to maximise our potential coverage. From these roughly 7,700 events, we downloaded data from every station between 90° and 135° epicentral distance. Data from stations at distances closer than the ray-theoretical $\mathrm{S_{diff}}$ cut-off ($\sim$100°) were included as very deep-diving S and ScS waves have direct sensitive to the CMB due to their wide Fresnel zone and can produce postcursors similar in character to $\mathrm{S_{diff}}+$. The combination of long-distance S/ScS and $\mathrm{S_{diff}}$ waveforms is sometimes referred to as S* (Wolf & Long, 2023).

We remove the instrument response, resample to 10 Hz, and detrend using TauP (Crotwell et al., 1999; Beyreuther et al., 2010). We then rotate the horizontal components to retrieve the transverse component, which we use for all analysis. We filtered the data using a Butterworth bandpass between 10–20 s of order 4. Traces were then kept on a per-station basis if the signal-to-noise ratio of the $\mathrm{S_{diff}}$ arrival was > 2.5, which we found to be a good compromise between removing the lowest quality traces and retaining the maximum possible information.

2.2.1 Dense Portions

It is impossible to conclusively observe the hyperbolic moveout typically associated with a ULVZ without a wide-angle receiver array ($> 5°$ aperture) spanning at least tens of stations. For this reason, within each event a search was undertaken for azimuthal segments of that event that would have a large enough number of stations within an azimuth range to identify $\mathrm{S_{diff}}$ postcursors. These ‘dense portions’ require at least 20 traces over a 20° azimuth window to begin, then the minimum and maximum azimuths adaptively grow and shrink to include all traces within a continuous azimuth range, where the edges of dense portions have a gap in azimuthal trace density to either side.

This process was applied to all events, totalling 17,470 dense portions. These were subsequently ordered by a combination of average signal-to-noise ratio and, to a lesser extent, total trace number. This ordering meant the information contained in each dense portion decreased as more dense portions were picked.

2.2.2 Picking $S_{diff}+$

During picking, each dense portion was displayed in the form of a record section where traces were binned by azimuth and aligned along the $\mathrm{S_{diff}}$ arrival time predicted by PREM, as is often presented in $\mathrm{S_{diff}}$ studies (e.g. Ni et al., 2005; Cottaar & Romanowicz, 2012). Traces were trimmed to between 20 s before and 100 s after the $\mathrm{S_{diff}}$ arrival time predicted by PREM. Earthquake information and absolute azimuths were obscured in order to anonymise events and eliminate a source of bias to geometries picked in previous studies.

Higher frequency bands (7–12 s, 5–8 s) were also used to allow for more accurate traveltime picks or for better positive and null detections in certain cases where possible. However, a majority of picks are based solely on data filtered between 10–20 s as data at higher frequencies tends to be noisier (Peterson, 1993). In some cases, $\mathrm{S_{diff}}+$ was found more clearly or solely in higher frequency bands (as in Martin et al., 2024).

Each azimuth was labelled with one of: positive postcursor detection (with an associated traveltime pick); negative postcursor detection (i.e. a definitive lack of postcursors); or uncertain (representing low quality data or high quality but ambiguous data).

Within positive and negative picks, a confidence was assigned (4 levels for positive, 2 levels for negative). A representative example of each of these levels is shown in Figure 2. The lowest confidence level of positive picks are deemed to be too uncertain, and are not used in the final output map or in subsequent analyses.

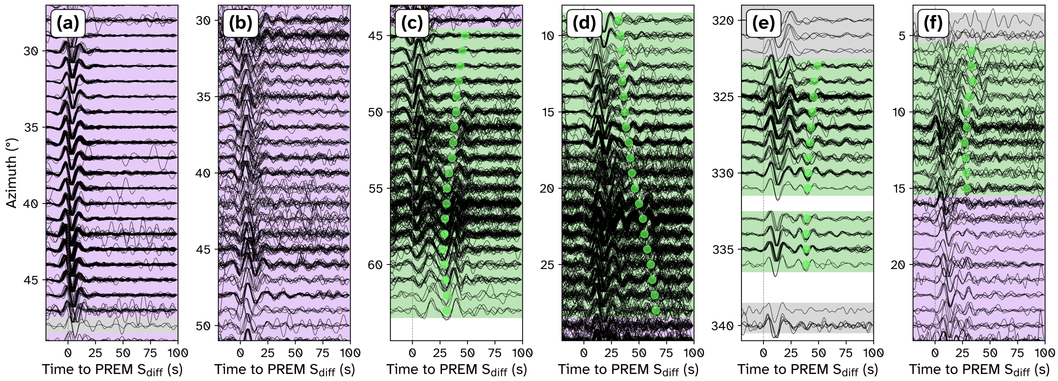

Figure 2. Examples of record sections showing negative (purple) and positive (green) S_{diff}+ detections at each of the 2 negative and 4 positive confidence levels. (a) and (b) show confident and uncertain null picks, respectively, while (c)–(f) show positive picks in decreasing order of confidence. (c), (d), and (f) also show regions of uncertain null picks. Azimuths highlighted in grey were deemed too low quality to pick.

The first 3,000 ordered dense portions were picked in their entirety. After this, we focused on two subsets of filtered data for the next 6,300 dense portions:

1. To increase unique geometries we look at earthquakes with fewer than 40 others in the dataset within 5°
2. To further increase coverage in the southern hemisphere, we look at earthquakes with fewer than 100 others in the dataset within 5° if the source is south of -15° latitude.

This led to a further 1,240 dense portions, bringing the total to 4,240 dense portions. At this point very little information was being added per dense portion (Figure S1), so picking was stopped.

Since only a minority of the total dense portions were picked (4,240 total, or 24%), there is significant scope for a machine learning model to be trained on the picked dataset and used to automatically generate picks for the remaining lower quality dense portions. Even though only 24% of the dense portions were picked, almost half of the total traces in the dataset were picked due to the ordering of the dense portions (2.04 million total, detailed in Table S1).

2.3 Collating Results

2.3.1 Accounting for Off-path Effects

S_{diff}+ caused by ULVZs does not necessarily represent structure along the great-circle path between the source and receiver, and in many cases backazimuths between S_{diff} and S_{diff}+ can vary by well beyond 10° (Cottaar & Romanowicz, 2012; Cottaar et al., 2022). A positive or negative pick can represent structures or a lack of structures multiple degrees to either side of the great circle path and must be accounted for.

For positive postcursor picks, traveltime picks that are close in azimuth and time to each other within a dense portion are grouped together and fitted with a hyperbola. Assuming a cylindrical ULVZ, the ULVZ will lie along the azimuth at the minimum of this hyperbola (Figure 1b). If the minimum of the hyperbola is well within the azimuth range of picks ($> 1°$ from either edge), then all the positive picks are condensed into a single line along the minimum of the hyperbola (Figure 3a). If the minimum is outside the azimuth range of picks, the positive picks are smeared over 10° to the side of the azimuth range closer to the minimum. If the minimum is within $< 1°$ from either edge, this smearing is reduced to 5°.

Negative picks are smeared over a range 10° to either side, as they imply both no ULVZ along the great circle and no ULVZ to some distance on either side (Figure 3b). The distances of both positive and negative smearing are based on previous $\mathrm{S_{diff}}$ studies, for which data and synthetics show $\mathrm{S_{diff}}$+ can be seen to 15–20° effective azimuth on either side of the ULVZ (Cottaar & Romanowicz, 2012; Z. Li et al., 2024), with 10° being a more conservative figure that is used in this study. The effect of the different smearing of positive and negative picks is that in the global map, positive regions are often tightly constrained and appear as thin lines, while negative regions appear much more diffuse.

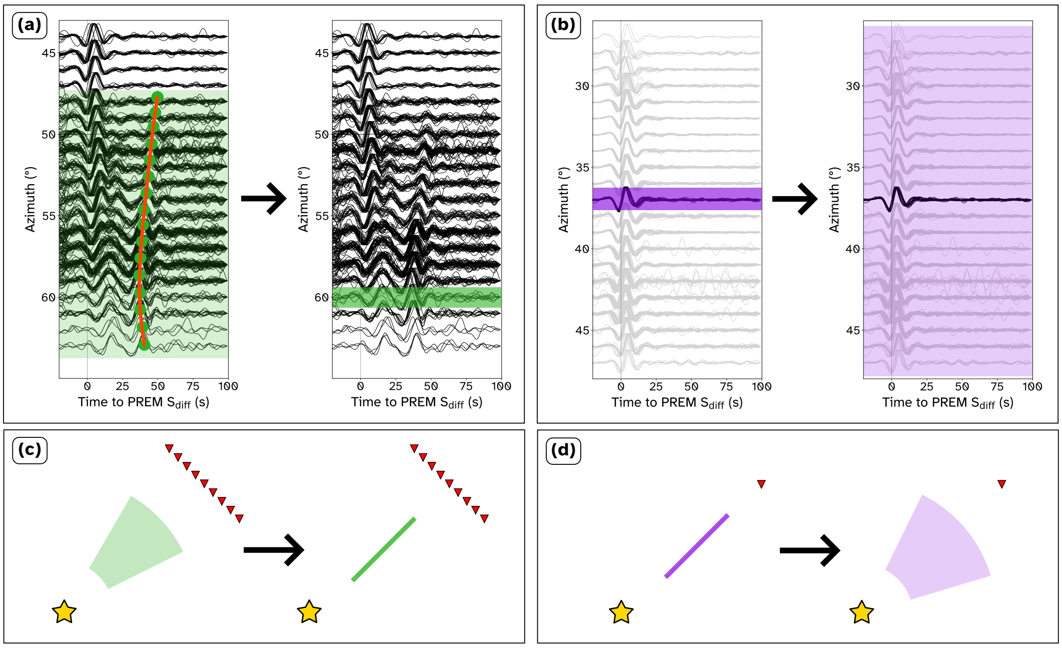

Figure 3. (a) Positive traveltime picks (green dots and highlight) are fit with a hyperbola (orange), and the weighting is condensed into a single line along the azimuth at the minimum. (b) A negative pick (purple highlight) for a single azimuth (in black) are smeared 10° to either side. Schematic versions of both cases are shown in (c) and (d), respectively.

2.3.2 Summing Picks into a Global Map

Lines are weighted by the number of stations that contributed to them divided by the azimuthal range over which have they been smeared, with positive detections being given positive weightings and negative detections being given negative weightings. For example, if 200 stations across 20° azimuth were picked as positive detections to form a hyperbola, the line along the minimum of that hyperbola would have a weighting of

+200. If an azimuth bin containing 63 stations was picked as a negative detection it would be split into 21 lines (10° to either side and the central line), each with a weighting of -3.

Lines are taken to be the portion of the infinite-frequency ray within 100 km of the CMB for each azimuth bin. These lines are then raytraced through an approximately equal-area grid of cells roughly 1° by 1° that cover the globe (following Bailey, 1956), Figure S2). Weightings of any positive or negative picks are summed to create a differential map of positive and negative detections. While the cells are not exactly the same area, median misfit from the target area is only 0.1%. These minor differences in cell sizes are ignored during statistical analyses.

2.3.3 Extracting ULVZ Locations

In the resulting map, positive detections create large areas of along-path smearing due to the long ray-path of S_{diff} for a single dense pick being unable to discriminate between ULVZ locations along that path. Previous ULVZs modelled with S_{diff} have most commonly been modelled as cylinders of varying radius (∼1°–9°), which is likely a much closer representation of their true morphology than what is expressed in our map. In cases of crossing data, we can locate the ULVZ with some confidence. For this reason, we performed an algorithm on our differential map to infer likely S_{diff}-ULVZ locations.

From our map, we take only the cells with a positive differential cell count and attempt to explain them with a set of individual S_{diff}-ULVZ locations. Our algorithm is as follows:

1. We place a ULVZ at the point on the map that has the highest weighted positive detection count summed over a region with radius of 5°.
2. We identify all $S_{\text{diff}}+$ detections that go through this ULVZ (defined as crossing the area within a radius of 7.5 degrees from its centre) and create a new map, excluding the entire ray paths of these explained $S_{\text{diff}}+$ detections.
3. We repeat this process until 99% of the original total positive cell count is matched.

For each ULVZ location placed, we find all nearby cells that contain at least 90% of the maximum central value, and take this to be our uncertainty in ULVZ centre location.

2.4 Statistical Analyses

We use the database of 44 hotspot locations collated by Steinberger (2000), based solely off surface features, to test the hypothesis that S_{diff}-ULVZs may be geographically linked to surface hotspots.

For each cell on our differential map, we calculate the distance from the centre of that cell to the closest hotspot (Figure 4a), then compare the distributions of distances to cells containing either positive or negative differentials. This lies in contrast to Yu and Garnero (2018), who calculate their distances in reverse: from each hotspot to the closest identified ULVZ. We chose to go from ULVZ to hotspot compared to going from each hotspot to the closest ULVZ as tomographic models do not suggest every hotspot being linked to a ULVZ, or being underlain by a mantle plume that is sourced from the lower mantle (Courtillot et al., 2003; French & Romanowicz, 2015; Marignier et al., 2020). Therefore we consider whether S_{diff}-ULVZs could be linked to hotspots, and not if all hotspots could be linked to S_{diff}-ULVZs.

In order to test the significance of our results we randomly rotate the hotspots 10,000 times and create distance distributions as we do with the map based on the observed data.

We follow the process of Schouten et al. (2024) and Domeier et al. (2016), based on work by Brannon (2002), to create random rotation matrices. These rotations are uniformly distributed, i.e. any point on our initial grid will cover the Earth uniformly after having been randomly rotated 10,000 times.

In order to account for our non-uniform global coverage, we divide the positive and negative distance distributions with the distance distribution of our coverage bin-by-bin. This creates a ratio that indicates whether positive or negative detections are under- or over-represented at each distance. We call this the 'representation ratio'. If positive or negative detections are placed uniformly within our coverage, we would expect the representation ratio to be 1 for all distance bins.

We also conduct tests based on the placement of the S_{diff}-ULVZs found from our location-finding algorithm to ascertain their significance. We place the same number of non-overlapping circular S_{diff}-ULVZs randomly around the globe. For each set of randomly-placed S_{diff}-ULVZs, we calculate the average distance from the centre to the nearest surface hotspot and compare this to the mean of the located S_{diff}-ULVZs. We conduct equivalent tests using the hotspot database of Morgan and Morgan (2007) and the deep-rooted plume database of French and Romanowicz (2015).

We also test the hypotheses that S_{diff}-ULVZs correlate with the edges of LLVPs, or if they are over-represented inside or outside LLVPs. We define LLVPs as regions with more than 3/5 votes of slow velocity, from the clustering analysis of Cottaar and Lekic (2016) which uses five global S-wave tomographic models (Figure 4b). Distances to LLVP edges are taken to be positive if outside an LLVP, and negative if inside. We also conduct equivalent tests where LLVP edges are defined directly from velocity reduction contours in the individual tomographic models GLAD-M35 (Cui et al., 2024) and REVEAL (Thrastarson et al., 2024).

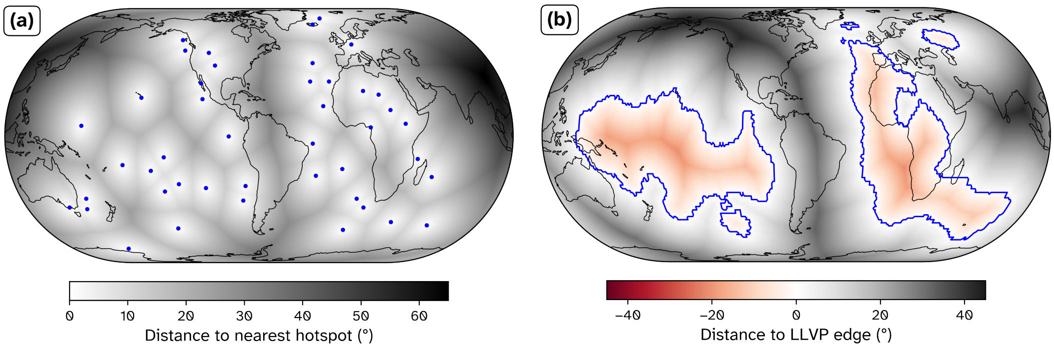

Figure 4. (a) Distance to the closest hotspot. Hotspots are shown as blue dots (Steinberger, 2000). (b) The equivalent for LLVP edges, where negative distances are inside LLVPs and positive distances are outside. LLVP edges (shown in blue) are based on the clustering analyses of tomographic models from Cottaar and Lekic (2016).

3 Results

3.1 Global ULVZ Presence and Absence

The differential map of global positive and negative ULVZ detections is shown in Figure 5. We achieve 99.8% coverage of the CMB, although if we require a minimum value of cell count for confident interpretation this coverage reduces (82.8% at 10; 63.7% at 50; 54.9% at 100; 30.3% at 500). Highs in coverage largely lie in regions surrounding North

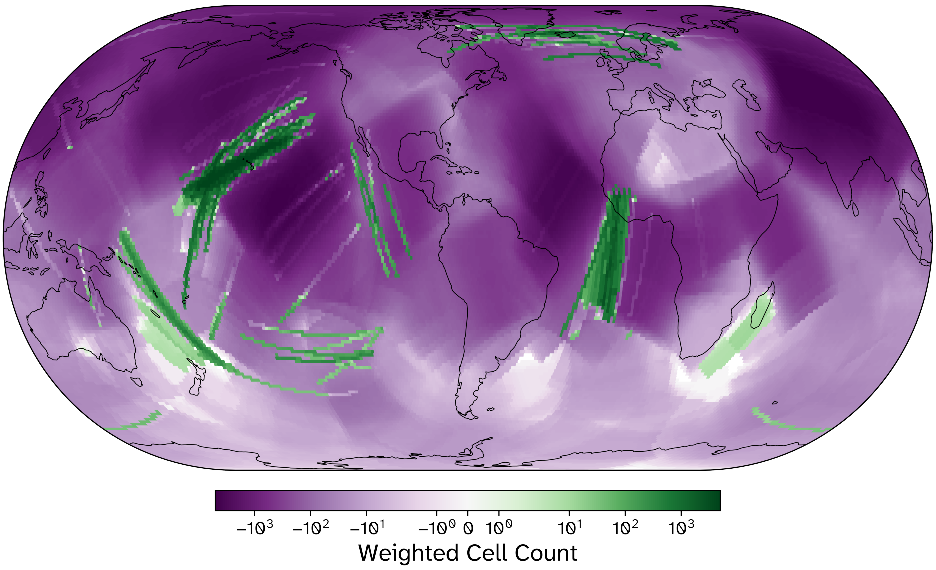

Figure 5. Global map of summed weighted cell count, where weightings from null detections are taken to have negative values and weightings from positive detections are taken to have positive values. Colours range from purple (null detection) through white (no coverage or ambiguous detection) to green (positive detection).

America and Europe, with the Northern Hemisphere having more coverage in general than the Southern Hemisphere. Differences in coverage are largely due to where large aperture broadband arrays required for S_{diff}+ detection are present, with the locations of high magnitude earthquakes playing a secondary role.

Positive detections cover 6.2% of the CMB. However, significant along-path smearing of positive detections is seen, notably along the two major directions near Hawaii: from New Zealand to Alaska; and from New Guinea to the mainland United States. Some regions of the map have narrow bands of continuous positive detections (e.g. near Hawaii or St. Helena), while others have more scattered detection paths (e.g. near Iceland, Galápagos or Pitcairn) potentially indicating some imprecision in the minimum azimuth of the S_{diff}+ traveltime hyperbola or in the assumption of a simple cylindrical ULVZ shape.

Aiming to match 99% of the positive cell count on the final map, six ULVZs locations are determined with the algorithm described in Section 2.3.3 (locations are given in Table S2). As shown in Figure 6 they lie near, in order that their locations were determined: Hawaii; St. Helena; Iceland; Galápagos; Vanuatu; and Pitcairn. ULVZ region names are derived from those used in the literature (Cottaar & Romanowicz, 2012; Davison et al., 2024; Yuan & Romanowicz, 2017; Cottaar et al., 2022; Z. Li et al., 2024, Martin et al., in review) . These six ULVZs cover approximately 1% of the CMB, which is far smaller than the positive coverage of 6.2% from the differential map. This is due to the smearing present in the main map, and the estimate of CMB coverage of the S_{diff}-ULVZs from the location-finding algorithm is more realistic.

3.2 Statistical Results

The representation ratio of observed positive and negative cells with respect to their closest hotspot, created using the method described in Section 3.2, is shown in Figure 7. Positive detections are only found within ∼25° of hotspots, and are overrepresented

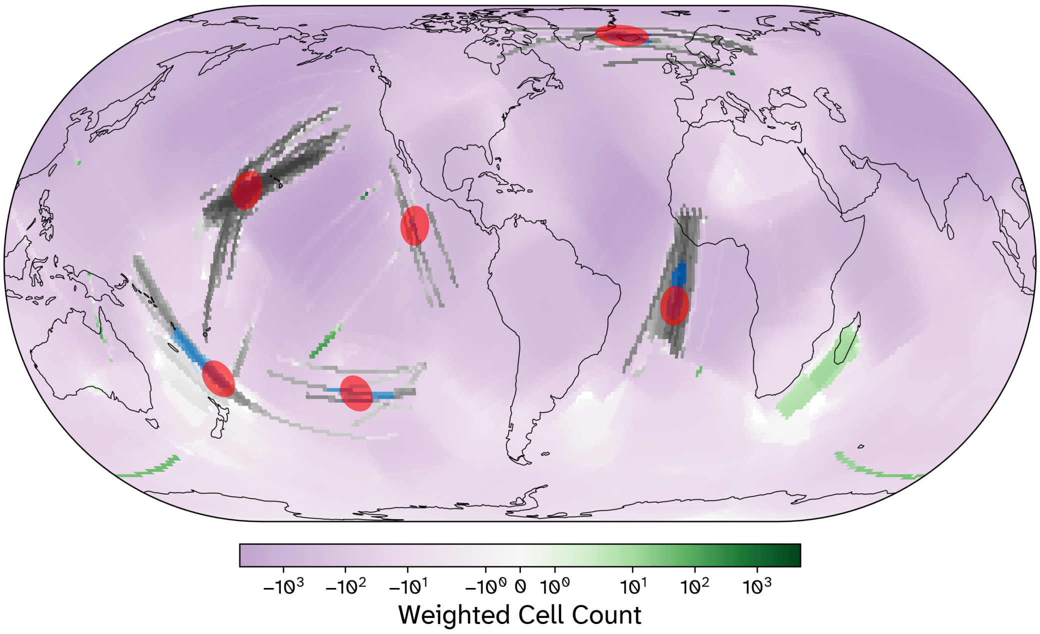

Figure 6. Locations of the six ULVZs found by the location-finding algorithm, shown as red circles. The background shows the weighted cell count from Figure 5. Grey areas are regions of positive detections explained by the six ULVZs. Blue shaded areas are regions of uncertainty on the location of the centre of each ULVZ.

within ∼20°. The representation ratio peaks close to the 95% confidence interval at ∼4° distance, meaning that approximately 2.5% of the random rotations give a more extreme peak. Negative detections show an opposite trend: they are underrepresented within ∼20°, and overrepresented beyond ∼25°. Most of the distribution is within the 95% confidence interval, with small peaks below and above at ∼10° and ∼30°, respectively.

The representation ratio of observed positive and negative cells with respect to LLVP edges is shown in Figure 8. Positive detections are only found within ∼20° of LLVP edges with a peak of the representation ratio centred on LLVP edges, raising slightly above the 99% confidence interval at 1° outside LLVPs, meaning that the observed distribution has a more extreme peak here than 99.5% of the randomly rotated versions. Positive detections are also overrepresented slightly within LLVPs. The opposite is found again for null picks: they are overrepresented far from LLVP edges and underrepresented close to LLVP edges.

We find that our set of algorithmically-located S_{diff}-ULVZs are closer on average to the nearest hotspot than 97.97% of the 10,000 randomly placed sets and closer on average to the nearest LLVP edge than 99.96% of the 10,000 randomly placed sets (Figure S4). Our set of algorithmically-determined S_{diff}-ULVZ locations therefore significantly correlate with surface hotspots and LLVP edges.

The results when using alternative hotspot databases (Figures S5-8) and alternative measures of LLVP edges derived directly from individual tomographic models (Figures S9-12) were similar.

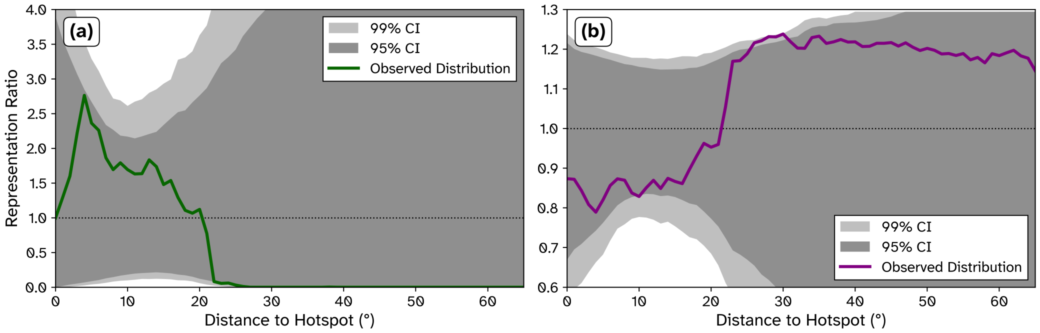

Figure 7. Representation ratio with distance to the nearest hotspot for the positive (a) and negative (b) portions of the differential map.

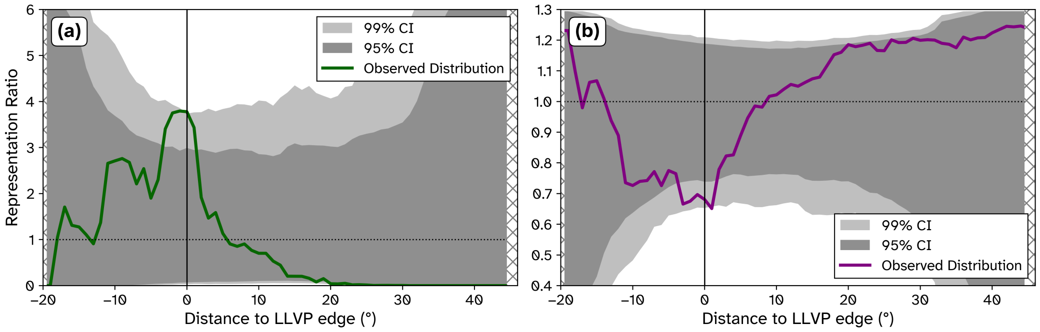

Figure 8. Equivalent of Figure 7 but for distances to LLVP edges. Positive distances are outside LLVPs and negative distances are within LLVPs. Hatched areas correspond to distances larger than the maximum possible for LLVP edges defined by Cottaar and Lekic (2016).

4 Discussion

4.1 Global ULVZ Distribution

The six algorithmically-located S_{diff}-ULVZs from our map have all been imaged in previous studies (Figure 9): e.g. Hawaii (J. Li et al., 2022; Z. Li et al., 2022; Cottaar & Romanowicz, 2012; Kim et al., 2020; Martin et al., 2023a); Iceland (Yuan & Romanowicz, 2017); Galápagos (Cottaar et al., 2022); St. Helena (Davison et al., 2024); Pitcairn (Z. Li et al., 2024); and Vanuatu (Martin et al., in review). Although exact locations are fairly unconstrained, our algorithmically-determined ULVZ locations match up well with previous S_{diff}-ULVZ studies. For example, the ULVZ under Hawaii is offset to the southwest like in previous studies (J. Li et al., 2022; Z. Li et al., 2022; Martin et al., 2023a; Jagt et al., 2024) and the ULVZ under Galápagos is offset to the west like in Cottaar et al. (2022).

However, there are some ULVZs previously mapped with S_{diff} missing from our global map. The ULVZ seen beneath the Himalayas (Wolf et al., 2024) is covered by one of the strongest negative regions on the map, though it is noted that there are some positive picks underneath the more prevalent negative picks (Figure 9). This ULVZ is reported to be far smaller than other ULVZs observed with S_{diff} (∼90 km in radius compared to 300–500 km), possibly limiting its detectability. Additionally, various ULVZ models have been proposed in the Central Pacific (Kim et al., 2020; Wolf & Long, 2023; Martin et al., 2024), and while there are very strong positive picks in the region (Figure 9), it remains overwhelmed by nearby negative picks. A possible explanation for this could be that the ULVZ in this region is more easily observed in higher frequencies such as 7–12 s, as reported by Martin et al. (2024), or 5–20 s, as reported by Wolf and Long (2023). This would mean it may only be seen intermittently in the 10–20 s filter band depending on signal-to-noise ratios and source properties, and so could be overwhelmed by nearby negative picks that have been horizontally smeared. The study of Kim et al. (2020) on the other hand observes S_{diff}+ at longer periods of 15–100 s, relating to a ULVZ which they suggest lies further South than the other studies.

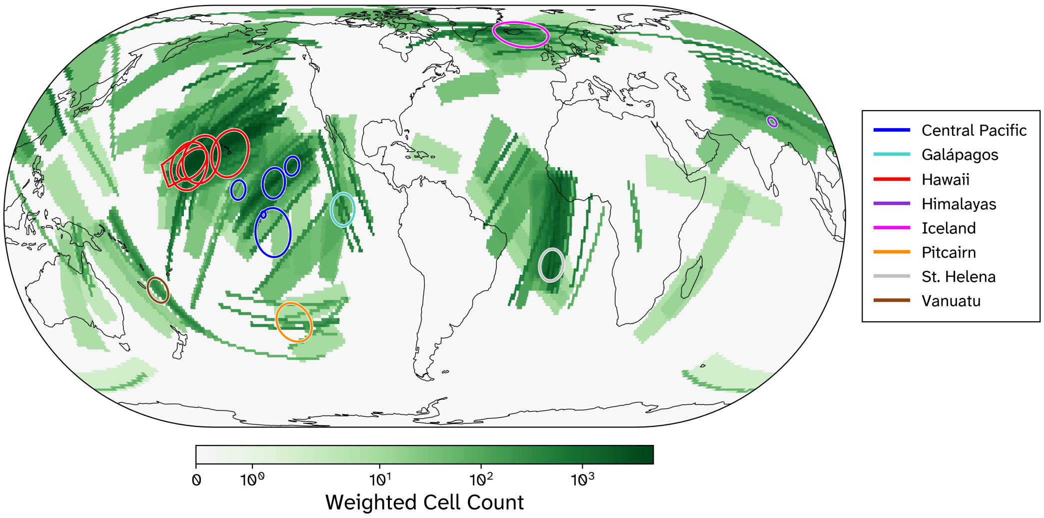

Figure 9. Equivalent of Figure 5 but only showing positive picks. S_{diff}-ULVZs mapped in previous studies are shown for comparison, with colours corresponding to different regions of detection: Central Pacific (Blue; Kim et al., 2020; Wolf & Long, 2023; Martin et al., 2024); Galápagos (Cyan; Cottaar et al., 2022); Hawaii (Red; J. Li et al., 2022; Z. Li et al., 2024; Cottaar & Romanowicz, 2012; Kim et al., 2020; Martin et al., 2023a); Himalayas (Purple; Wolf et al., 2024); Iceland (Magenta; Yuan & Romanowicz, 2017); Pitcairn (Orange; Z. Li et al., 2024); St. Helena (Grey; Davison et al., 2024); Vanuatu (Brown; Martin et al., in review).

Direct comparisons between our map and the global map of ULVZs using $SP_{\mathrm{diff}}KS$ by Thorne et al. (2021) are difficult for two reasons. Firstly, our coverage is largely complementary to theirs — they have coverage highs underneath the continental US, South America, and the Western Pacific, which are all regions of relatively low coverage in our map. Of the regions that are shared, such as underneath East Asia, we do not find evidence of the heterogeneities observed in their map. Secondly, significant differences in the sensitivities of S_{diff} and $SP_{\mathrm{diff}}KS$ mean that ULVZs observed by the two phases may be hard to detect or even invisible to one another. The Samoa mega-ULVZ (Thorne et al., 2013; Krier et al., 2021) exemplifies these difficulties — it is the region with the highest likelihood of ULVZ presence in the map of Thorne et al. (2021), but is missing from our map. The surrounding region has less than 100 weighted cell count and so lies in an area of low coverage in our map. There are only two major geometries than would sample this area: New Zealand to Alaska, along which the Hawaiian ULVZ may obscure any other signals; and the East Pacific Rise to East Asia, along which the Vanuatu ULVZ lies. The latter geometry was explored by Martin et al. (in review), who found that S_{diff}+ expected by the Samoa mega-ULVZ were not found in record sections. This may be explained by the differing sensitivities of the two phases, or potentially the elongate morphology of the Samoa mega-ULVZ which may make detection with S_{diff} more difficult.

Réunion, Papua, and the Southern Indian Ocean all show evidence for $S_{\text{diff}}+$ presence, albeit with much more limited observations than other S_{diff}-ULVZs. All three regions also lie along the edges of LLVPs. The Southern Indian Ocean has been targeted with S_{diff} studies previously to argue for sharp LLVP edges (Ni et al., 2002; To et al., 2005), which can produce similar postcursors to those associated with ULVZs (Wolf et al., 2025). In our map, we assume that all postcursors are formed by ULVZs as opposed to sharp LLVP edges, but the extent to which these two features can be distinguished by S_{diff} is uncertain, and requires further modelling.

Null detections cover 93.7% of the core-mantle boundary, often as strong in cell count as the strongest positive detection regions. A large majority of the CMB is devoid of S_{diff}-ULVZs, although smaller ULVZs not visible to S_{diff} may still be present in these null regions. Strong negative regions lie along LLVP edges (Central Pacific, Central Atlantic), inside LLVPs (Central Africa), and outside LLVPs (Northern Pacific, Asia), suggesting that S_{diff}-ULVZs do not line LLVP edges, but occur at isolated regions along them. Similarly, most hotspots globally are not underlain by an S_{diff}-ULVZ. For example, the Afar and Cape Verde hotspots notably have high buoyancy fluxes (Sleep, 1990; Hoggard et al., 2020) and are imaged to have deep plume roots (Courtillot et al., 2003; French & Romanowicz, 2015), but are present in regions of null detections in our map. However, we note that if the lowest quality positive detections are added, $S_{\text{diff}}+$ are seen under Cape Verde and Eastern Africa, as well as Nova Scotia (Figures S13 and S14f).

The largest drawback of our methodology is the human element and inherent irreproducibility of the picking itself. Although steps were taken to remove bias during picking, such as obscuring event and receiver locations, there still remains significant subjectivity in picking. Hand-picking of seismic data remains prevalent, not just in the case of detecting ULVZs with S_{diff}, but it would be interesting to compare this map to another created by automated methods also using S_{diff} (e.g. Wolf et al., 2025).

4.2 Relationships with Hotspots and LLVP Edges

Positive detections are found significantly closer than null detections to both hotspots and LLVP edges in our map.

In all our tests, we find a clearer correlation between S_{diff}-ULVZs and LLVP edges compared to that between ULVZs and surface hotspots. A weaker correlation with hotspots may be expected if mantle plumes are not purely vertical but are inclined or have lateral deviations part of the way up their ascent, as is seen in recent tomographic models (e.g. Koppers et al., 2021; French & Romanowicz, 2015; Cui et al., 2024). This would give a lateral offset between surface and CMB locations even if there is a continuous plume between the two.

The debate is open as to whether ULVZs can be linked to isotopic signatures measured at ocean island basalts (e.g. Cottaar et al., 2022; Herret et al., 2023). Anomalies in helium (e.g. Stuart et al., 2003; Class & Goldstein, 2005; Jackson et al., 2017) and tungsten (e.g. Rizo et al., 2019; Mundl-Petermeier et al., 2020; Ferrick & Korenaga, 2023; Horton et al., 2023) have been proposed as evidence of primordial material or a signature from the core. Recently anomalies in ruthenium have been observed that point further toward a potential core signature (Messling et al., 2025). However, variations in isotope systematics suggest that different primordial domains must be sampled over time (Mundl-Petermeier et al., 2019; Peters et al., 2025). The ULVZs are one potential domain that could store a primordial or core signature.

Of the six mapped ULVZs in this study, Hawaii, Iceland, and and Galápagos have mantle plumes amongst the highest buoyancy fluxes (Hoggard et al., 2020) and show extreme OIB isotopes in both helium (Jackson et al., 2017) and tungsten (Mundl-Petermeier et al., 2020). The Pitcairn ULVZ lies near the Pitcairn, Macdonald, and Easter hotspots, all three of which show evidence of anomalous helium signatures and some tungsten signatures. The St. Helena ULVZ lies near the St. Helena and Ascension hotspots, for which the helium signal might be masked by recycled crust and the tungsten signature has not been tested (Davison et al., 2024). The Vanuatu ULVZ is further from surface hotspots, although may potentially feed into the Samoa hotspot, which has anomalous OIB isotopes and a high buoyancy flux. However, a large ULVZ has been observed closer to Samoa using $\mathrm{SP_{diff}KS}$ (Thorne et al., 2013).

We observe a strong relationship between our mapped ULVZs and LLVP edges, which is also supported by geodynamic modelling of dense and compositionally-distinct material that potentially makes up the ULVZs. In models, dense material is swept towards LLVP edges, where it accumulates to form ULVZs (McNamara et al., 2010; M. Li et al., 2017; X. Liu et al., 2024), aligning well with the $\mathrm{S_{diff}}$-ULVZ locations shown in this study. Other types of seismic phases find ULVZ heterogeneity in a variety of morphologies outside LLVPs (e.g. Hansen et al., 2020; Thorne et al., 2021; Su et al., 2024). It is possible that the large-scale $\mathrm{S_{diff}}$-ULVZs represent older ULVZs which have had more time to both accumulate material and relocate towards LLVP edges, while smaller ULVZs seen with other phases may be younger and in the process of moving towards LLVP edges.

5 Conclusions

We have created a map of the presence and absence of $\mathrm{S_{diff}}$-ULVZs on the CMB by handpicking over 2 million waveforms for postcursors to the phase $\mathrm{S_{diff}}$, achieving near-global coverage. The presence and locations of six previously-identified $\mathrm{S_{diff}}$-ULVZs are reconfirmed, with some evidence for newly-discovered regions of $\mathrm{S_{diff}}$-ULVZ presence. A large majority of the CMB is found to be absent of $\mathrm{S_{diff}}$-ULVZs, especially that which is furthest from LLVPs. $\mathrm{S_{diff}}$-ULVZs lie along the edges of LLVPs and appear to be correlated with the locations of surface hotspots via plume conduits, possibly with mid-mantle deflections. However, with far fewer $\mathrm{S_{diff}}$-ULVZs than hotspots, it does not appear that every deep-rooted plume necessarily has an $\mathrm{S_{diff}}$-ULVZ at its root.

Open Research Section

The facilities of IRIS Data Services (www.iris.edu), and specifically the IRIS Data Management Center, were used for access to waveforms and related metadata. IRIS Data Services are funded through the Seismological Facilities for the Advancement of Geoscience (SAGE) Award of the National Science Foundation under Cooperative Support Agreement EAR-1851048. Data from the F-net and Hi-net networks were made freely available by National Research Institute for Earth Science and Disaster Resilience (Okada et al., 2004). Data from NIED was downloaded using HinetPy (Tian, 2024) and FnetPy (https://github.com/seisman/FnetPy). Networks that provided the waveform data used in this study can be found in Supplementary Information Text S3. Earthquake parameters were used from the Global CMT Project (www.globalcmt.org). Waveform processing was performed using ObsPy version 1.4.1 (Beyreuther et al., 2010). Data containing the weighted cell count at each confidence level for each cell of the differential map can be found in Supplementary Material B. Data and codes will be made available by JA upon request.

Conflict of Interest declaration

The authors declare there are no conflicts of interest for this manuscript.

Acknowledgments

The authors would like to thank past and present members of the University of Cambridge Earth Sciences Department, especially Stuart Russell, David Al-Attar, and Sergei Lebedev, who have provided helpful and insightful scientific discussions; and Neil Marjoram and John Parry for technical support.

JA, CM and SC received funding from the European Research Council (ERC) under the European Union's Horizon 2020 research and innovation programme (grant agreement No. 804071 -ZoomDeep). JA and SC received funding from the Natural Environment Research Council (NE/S007164/1 and NE/V018213/1, respectively). CM received funding from a Vici award (grant number 016.160.310/526) from the Dutch Research Council (NWO).

References

Avants, M., Lay, T., & Garnero, E. J. (2006). A new probe of ULVZ S-wave velocity structure: Array stacking of ScS waveforms. *Geophysical Research Letters*, *33*(7).

Bailey, H. P. (1956). Two grid systems that divide the entire surface of the Earth into quadrilaterals of equal area. *Eos, Transactions American Geophysical Union*, *37*(5), 628–635.

Beyreuther, M., Barsch, R., Krischer, L., Megies, T., Behr, Y., & Wassermann, J. (2010). ObsPy: A Python toolbox for seismology. *Seismological Research Letters*, *81*(3), 530–533.

Brannon, R. M. (2002). ROTATION: A Review of Useful Theorems Involving Proper Orthogonal Matrices Referenced to Threedimensional Physical Space. *Computational Physics and Mechanics*.

Brown, S. P., Thorne, M. S., Miyagi, L., & Rost, S. (2015). A compositional origin to ultralow-velocity zones. *Geophysical Research Letters*, *42*(4), 1039–1045.

Buffett, B. A., Garnero, E. J., & Jeanloz, R. (2000). Sediments at the top of Earth's core. *Science*, *290*(5495), 1338–1342.

Class, C., & Goldstein, S. L. (2005). Evolution of helium isotopes in the Earth's mantle. *Nature*, *436*(7054), 1107–1112.

Cottaar, S., & Lekic, V. (2016). Morphology of seismically slow lower-mantle structures. *Geophysical Supplements to the Monthly Notices of the Royal Astronomical Society*, *207*(2), 1122–1136.

Cottaar, S., Martin, C., Li, Z., & Parai, R. (2022). The root to the Galápagos mantle plume on the core-mantle boundary. *Seismica*, *1*(1).

Cottaar, S., & Romanowicz, B. (2012). An unusally large ULVZ at the base of the mantle near Hawaii. *Earth and Planetary Science Letters*, *355*, 213–222.

Courtillot, V., Davaille, A., Besse, J., & Stock, J. (2003). Three distinct types of hotspots in the Earth's mantle. *Earth and Planetary Science Letters*, *205*(3-4), 295–308.

Crotwell, H. P., Owens, T. J., Ritsema, J., et al. (1999). The TauP Toolkit: Flexible seismic travel-time and ray-path utilities. *Seismological Research Letters*, *70*, 154–160.

Cucchiaro, A., Flament, N., Arnould, M., & Cressie, N. (2025). Large volcanic eruptions are mostly sourced above mobile basal mantle structures. *Communications Earth & Environment*, *6*(1), 538.

Cui, C., Lei, W., Liu, Q., Peter, D., Bozdağ, E., Tromp, J., ... Pugmire, D. (2024). GLAD-M35: a joint P and S global tomographic model with uncertainty quantification. *Geophysical Journal International*, *239*(1), 478–502.

Dannberg, J., Myhill, R., Gassmöller, R., & Cottaar, S. (2021). The morphology, evolution and seismic visibility of partial melt at the core–mantle boundary: Implications for ULVZs. *Geophysical Journal International*, *227*(2), 1028–

1059.

Davison, S., Martin, C., Parai, R., & Cottaar, S. (2024). Ultra-low velocity zone beneath the Atlantic near St. Helena. *Geochemistry, Geophysics, Geosystems*, *25*(7), e2024GC011559.

Dobrosavljevic, V. V., Sturhahn, W., & Jackson, J. M. (2019). Evaluating the role of iron-rich (Mg, Fe) O in ultralow velocity zones. *Minerals*, *9*(12), 762.

Dobson, D. P., & Brodholt, J. P. (2005). Subducted banded iron formations as a source of ultralow-velocity zones at the core–mantle boundary. *Nature*, *434*(7031), 371–374.

Domeier, M., Doubrovine, P. V., Torsvik, T. H., Spakman, W., & Bull, A. L. (2016). Global correlation of lower mantle structure and past subduction. *Geophysical Research Letters*, *43*(10), 4945–4953.

Dziewonski, A. M., & Anderson, D. L. (1981). Preliminary reference Earth model. *Physics of the earth and planetary interiors*, *25*(4), 297–356.

Ferrick, A. L., & Korenaga, J. (2023). Long-term core–mantle interaction explains W-He isotope heterogeneities. *Proceedings of the National Academy of Sciences*, *120*(4), e2215903120.

French, S. W., & Romanowicz, B. (2015). Broad plumes rooted at the base of the Earth's mantle beneath major hotspots. *Nature*, *525*(7567), 95–99.

Hansen, S. E., Carson, S. E., Garnero, E. J., Rost, S., & Yu, S. (2020). Investigating ultra-low velocity zones in the southern hemisphere using an Antarctic dataset. *Earth and Planetary Science Letters*, *536*, 116142.

Hauser, J., Sambridge, M., & Rawlinson, N. (2008). Multiarrival wavefront tracking and its applications. *Geochemistry, Geophysics, Geosystems*, *9*(11).

Helmberger, D., Wen, L., & Ding, X. (1998). Seismic evidence that the source of the Iceland hotspot lies at the core–mantle boundary. *Nature*, *396*(6708), 251–255.

Hernlund, J. W., & Tackley, P. J. (2007). Some dynamical consequences of partial melting in Earth's deep mantle. *Physics of the Earth and Planetary Interiors*, *162*(1-2), 149–163.

Herret, M.-T., Peters, B. J., Kim, D., Castillo, P., & Mundl-Petermeier, A. (2023). Decoupling of short-lived radiogenic and helium isotopes in the Marquesas hotspot. *Chemical Geology*, *640*, 121727.

Hoggard, M. J., Parnell-Turner, R., & White, N. (2020). Hotspots and mantle plumes revisited: Towards reconciling the mantle heat transfer discrepancy. *Earth and Planetary Science Letters*, *542*, 116317.

Horton, F., Asimow, P., Farley, K., Curtice, J., Kurz, M., Blusztajn, J., … Boyes, X. (2023). Highest terrestrial 3He/4He credibly from the core. *Nature*, *623*(7985), 90–94.

Hutko, A. R., Lay, T., & Revenaugh, J. (2009). Localized double-array stacking analysis of PcP: D ″ and ULVZ structure beneath the Cocos plate, Mexico, central Pacific, and north Pacific. *Physics of the Earth and Planetary Interiors*, *173*(1-2), 60–74.

Jackson, M., Konter, J., & Becker, T. (2017). Primordial helium entrained by the hottest mantle plumes. *Nature*, *542*(7641), 340–343.

Jagt, L., Martin, C., Millet, F., Russell, S., & Cottaar, S. (2024). Pdiff Postcursors from the Base of the Hawaiian ULVZ. *The Seismic Record*, *4*(3), 204–213.

Jenkins, J., Mousavi, S., Li, Z., & Cottaar, S. (2021). A high-resolution map of Hawaiian ULVZ morphology from ScS phases. *Earth and Planetary Science Letters*, *563*, 116885.

Kim, D., Lekić, V., Ménard, B., Baron, D., & Taghizadeh-Popp, M. (2020). Sequencing seismograms: A panoptic view of scattering in the core-mantle boundary region. *Science*, *368*(6496), 1223–1228.

Koppers, A. A., Becker, T. W., Jackson, M. G., Konrad, K., Müller, R. D., Romanowicz, B., … Whittaker, J. M. (2021). Mantle plumes and their role in

Earth processes. *Nature Reviews Earth & Environment*, *2*(6), 382–401.

Krier, J., Thorne, M. S., Leng, K., & Nissen-Meyer, T. (2021). A compositional component to the Samoa ultralow-velocity zone revealed through 2-and 3-D waveform modeling of SKS and SKKS differential travel-times and amplitudes. *Journal of Geophysical Research: Solid Earth*, *126*(7), e2021JB021897.

Lai, V. H., Helmberger, D. V., Dobrosavljevic, V. V., Wu, W., Sun, D., Jackson, J. M., & Gurnis, M. (2022). Strong ULVZ and slab interaction at the northeastern edge of the Pacific LLSVP favors plume generation. *Geochemistry, Geophysics, Geosystems*, *23*(2), e2021GC010020.

Li, M., McNamara, A. K., Garnero, E. J., & Yu, S. (2017). Compositionally-distinct ultra-low velocity zones on Earth's core-mantle boundary. *Nature Communications*, *8*(1), 177.

Li, Z., Martin, C., & Cottaar, S. (2024). Seismic observation of a new ULVZ beneath the Southern Pacific. *Journal of Geophysical Research: Solid Earth*, *129*(4), e2023JB026941.

Liu, J., Hu, Q., Young Kim, D., Wu, Z., Wang, W., Xiao, Y., ... others (2017). Hydrogen-bearing iron peroxide and the origin of ultralow-velocity zones. *Nature*, *551*(7681), 494–497.

Liu, J., Li, J., Hrubiak, R., & Smith, J. S. (2016). Origins of ultralow velocity zones through slab-derived metallic melt. *Proceedings of the National Academy of Sciences*, *113*(20), 5547–5551.

Liu, X., Tian, F., Li, J., Li, Y., & Sun, W. (2024). The evolution of dense ULVZs originating outside LLSVPs and implications for dynamics at LLSVP margins. *Journal of Geophysical Research: Solid Earth*, *129*(12), e2024JB028972.

Marignier, A., Ferreira, A. M., & Kitching, T. (2020). The probability of mantle plumes in global tomographic models. *Geochemistry, Geophysics, Geosystems*, *21*(9), e2020GC009276.

Martin, C., Bodin, T., & Cottaar, S. (2023a). Mapping structures on the core–mantle boundary using Sdiff postcursors: Part II. Application to the Hawaiian ULVZ. *Geophysical Journal International*, *235*(3), 2399–2409.

Martin, C., Bodin, T., & Cottaar, S. (2023b). Mapping structures on the core–mantle boundary using Sdiff postcursors: Part I. Method and Validation. *Geophysical Journal International*, *235*(3), 2385–2398.

Martin, C., Russell, S., & Cottaar, S. (2024). Detection of a ULVZ in the Central Pacific using high frequency Sdiff postcursors. *Earth and Planetary Science Letters*, *648*, 119028.

McNamara, A. K. (2019). A review of large low shear velocity provinces and ultra low velocity zones. *Tectonophysics*, *760*, 199–220.

McNamara, A. K., Garnero, E. J., & Rost, S. (2010). Tracking deep mantle reservoirs with ultra-low velocity zones. *Earth and Planetary Science Letters*, *299*(1-2), 1–9.

Messling, N., Willbold, M., Kallas, L., Elliott, T., Fitton, J. G., Müller, T., & Geist, D. (2025). Ru and W isotope systematics in ocean island basalts reveals core leakage. *Nature*, 1–5.

Morgan, W. J., & Morgan, J. P. (2007). Plate velocities in the hotspot reference frame. *Plates, Plumes, and Planetary Processes*, *430*, 65.

Muir, J. M., & Brodholt, J. P. (2016). Ferrous iron partitioning in the lower mantle. *Physics of the Earth and Planetary Interiors*, *257*, 12–17.

Mundl, A., Touboul, M., Jackson, M. G., Day, J. M., Kurz, M. D., Lekic, V., ... Walker, R. J. (2017). Tungsten-182 heterogeneity in modern ocean island basalts. *Science*, *356*(6333), 66–69.

Mundl-Petermeier, A., Walker, R., Fischer, R., Lekic, V., Jackson, M., & Kurz, M. D. (2020). Anomalous 182W in high 3He/4He ocean island basalts: fingerprints of Earth's core? *Geochimica et Cosmochimica Acta*, *271*, 194–211.

Mundl-Petermeier, A., Walker, R., Jackson, M., Blichert-Toft, J., Kurz, M., &

Halldórsson, S. A. (2019). Temporal evolution of primordial tungsten-182 and 3He/4He signatures in the Iceland mantle plume. *Chemical Geology*, *525*, 245–259.

Ni, S., Tan, E., Gurnis, M., & Helmberger, D. (2002). Sharp sides to the African superplume. *science*, *296*(5574), 1850–1852.

Ni, S., V. Helmberger, D., & Tromp, J. (2005). Three-dimensional structure of the African superplume from waveform modelling. *Geophysical Journal International*, *161*(2), 283–294.

Ohtani, E., & Maeda, M. (2001). Density of basaltic melt at high pressure and stability of the melt at the base of the lower mantle. *Earth and Planetary Science Letters*, *193*(1-2), 69–75.

Okada, Y., Kasahara, K., Hori, S., Obara, K., Sekiguchi, S., Fujiwara, H., & Yamamoto, A. (2004). Recent progress of seismic observation networks in Japan—Hi-net, F-net, K-NET and KiK-net. *Earth, Planets and Space*, *56*, xv–xxviii.

Peters, B. J., Mundl-Petermeier, A., & Larsen, L. M. (2025). Variable sampling of distinct ancient mantle domains by the Iceland mantle plume over its 62 Ma eruption history. *Chemical Geology*, 122882.

Peterson, J. R. (1993). *Observations and modeling of seismic background noise* (Tech. Rep.). US Geological Survey.

Rizo, H., Andrault, D., Bennett, N., Humayun, M., Brandon, A., Vlastélic, I., ... Murphy, D. (2019). 182W evidence for core-mantle interaction in the source of mantle plumes. *Geochemical Perspectives Letters*, *11*, 6–11.

Rondenay, S., & Fischer, K. M. (2003). Constraints on localized core-mantle boundary structure from multichannel, broadband SKS coda analysis. *Journal of Geophysical Research: Solid Earth*, *108*(B11).

Rost, S., Garnero, E. J., Williams, Q., & Manga, M. (2005). Seismological constraints on a possible plume root at the core–mantle boundary. *Nature*, *435*(7042), 666–669.

Schouten, T. L., Gebraad, L., Noe, S., Gülcher, A. J., Thrastarson, S., van Herwaarden, D.-P., & Fichtner, A. (2024). Full-waveform inversion reveals diverse origins of lower mantle positive wave speed anomalies. *Scientific Reports*, *14*(1), 26708.

Sleep, N. H. (1990). Hotspots and mantle plumes: Some phenomenology. *Journal of Geophysical Research: Solid Earth*, *95*(B5), 6715–6736.

Steinberger, B. (2000). Plumes in a convecting mantle: Models and observations for individual hotspots. *Journal of Geophysical Research: Solid Earth*, *105*(B5), 11127–11152.

Stuart, F. M., Lass-Evans, S., Godfrey Fitton, J., & Ellam, R. M. (2003). High 3He/4He ratios in picritic basalts from Baffin Island and the role of a mixed reservoir in mantle plumes. *Nature*, *424*(6944), 57–59.

Su, Y., Ni, S., Zhang, B., Chen, Y., Wu, W., Li, M., ... Sun, D. (2024). Detections of ultralow velocity zones in high-velocity lowermost mantle linked to subducted slabs. *Nature Geoscience*, *17*(4), 332–339.

Thorne, M. S., Garnero, E. J., Jahnke, G., Igel, H., & McNamara, A. K. (2013). Mega ultra low velocity zone and mantle flow. *Earth and Planetary Science Letters*, *364*, 59–67.

Thorne, M. S., Leng, K., Pachhai, S., Rost, S., Wicks, J., & Nissen-Meyer, T. (2021). The most parsimonious ultralow-velocity zone distribution from highly anomalous SPdKS waveforms. *Geochemistry, Geophysics, Geosystems*, *22*(1), e2020GC009467.

Thorne, M. S., Pachhai, S., & Garnero, E. J. (2024). Effects of 2.5-D ultra-low and ultra-high velocity zones on flip-reverse-stacking (FRS) of the ScS wavefield. *Geophysical Journal International*, *239*(2), 1038–1062.

Thrastarson, S., van Herwaarden, D.-P., Noe, S., Josef Schiller, C., & Fichtner, A.

(2024). REVEAL: A global full-waveform inversion model. *Bulletin of the Seismological Society of America*, *114*(3), 1392–1406.

Tian, D. (2024). HinetPy: A Python package for accessing and processing NIED Hi-net seismic data. *Journal of Open Source Software*, *9*(98), 6840.

To, A., Romanowicz, B., Capdeville, Y., & Takeuchi, N. (2005). 3D effects of sharp boundaries at the borders of the African and Pacific Superplumes: Observation and modeling. *Earth and Planetary Science Letters*, *233*(1-2), 137–153.

Torsvik, T. H., Smethurst, M. A., Burke, K., & Steinberger, B. (2006). Large igneous provinces generated from the margins of the large low-velocity provinces in the deep mantle. *Geophysical Journal International*, *167*(3), 1447–1460.

Wen, L. (2000). Intense seismic scattering near the Earth's core-mantle boundary beneath the Comoros hotspot. *Geophysical research letters*, *27*(22), 3627–3630.

Wen, L., & Helmberger, D. V. (1998). Ultra-low velocity zones near the core-mantle boundary from broadband PKP precursors. *Science*, *279*(5357), 1701–1703.

Williams, Q., & Garnero, E. J. (1996). Seismic evidence for partial melt at the base of Earth's mantle. *Science*, *273*(5281), 1528–1530.

Wolf, J., Garnero, E., Schwarz, B., Leng, K., Luo, Y., Maass, R., & West, J. D. (2025). Detection of lowermost mantle heterogeneity using seismic migration of diffracted S-waves. *Journal of Geophysical Research: Solid Earth*, *130*(6), e2025JB031367.

Wolf, J., & Long, M. D. (2023). Lowermost mantle structure beneath the central Pacific Ocean: Ultralow velocity zones and seismic anisotropy. *Geochemistry, Geophysics, Geosystems*, *24*(6), e2022GC010853.

Wolf, J., Long, M. D., & Frost, D. A. (2024). Ultralow velocity zone and deep mantle flow beneath the Himalayas linked to subducted slab. *Nature Geoscience*, *17*(4), 302–308.

Yu, S., & Garnero, E. J. (2018). Ultralow velocity zone locations: A global assessment. *Geochemistry, Geophysics, Geosystems*, *19*(2), 396–414.

Yuan, K., & Romanowicz, B. (2017). Seismic evidence for partial melting at the root of major hot spot plumes. *Science*, *357*(6349), 393–397.

Zhang, Y., Ritsema, J., & Thorne, M. S. (2009). Modeling the ratios of SKKS and SKS amplitudes with ultra-low velocity zones at the core-mantle boundary. *Geophysical Research Letters*, *36*(19).

JOURNAL OF GEOPHYSICAL RESEARCH

Supporting Information for ”Global presence and absence of ultra-low velocity zones as seen by Sdiff postcursors”

J. R. Atkins[1], C. Martin[2], S. Cottaar[1]

[1]Bullard Laboratories, Department of Earth Sciences, University of Cambridge, CB3 0EZ, UK

[2]Department of Geosciences, Utrecht University, 3854 CB, Netherlands

Contents of this file

1. Figures S1 to S14
2. Tables S1 and S2
3. Text S1 to S3

Text S1 — Information about Additional Methodological Figures and Tables

Figure S1 shows the number of traces picked per dense portion during the picking process. The numbers decrease as more dense portions were picked due to the ordering described in Section 2.2, which placed dense portions with large numbers of high quality traces first. Due to this decrease, we change strategy after 3,000 dense portions, after which we only pick dense portions with uncommon geometries, sampling more generously in the southern Hemisphere. This leads to a steeper decrease in picked numbers, but

---

Corresponding author: J. R. Atkins, Bullard Laboratories, University of Cambridge, CB3 0EZ, UK. (jra64@cam.ac.uk)

provides increased global coverage. Table S1 gives the total number of picks for each level of confidence for positive and null observations (which are negative observations on our maps).

An equal-area grid is critical for our statistical analyses. A map showing the construction of the approximately equal grid is shown in Figure S2. All cells, even those at high latitudes, have very similar shapes and areas.

Text S2 — Information about Additional Results Figures and Tables

The locations of the six algorithmically-determined $\mathrm{S_{diff}}$-ULVZs and their approximate regions are shown in Table S2.

The distribution of the distances for positive and negative summed grid points relative to hotspots and the edges of LLVPs is shown in Figure S3. In this case, the distributions are not divided by the distance distribution of all grid points (like is done for Figures 7 and 8). In the case of hotspots, positive detections lie on average 11.2° from the closest hotspot, while negative detections lie on average 25.7° away. In the case of LLVP edges, positive detections lie on average 0.4° within LLVP edges, while negative detections lie on average 14.5° outside. In both cases, the standard deviation of the negative detection distribution is large and overlaps with the standard deviation of the positive detections. Both still agree with the findings that $\mathrm{S_{diff}}$-ULVZs are found near both hotspots and LLVP edges.

Comparisons between the average distance to the nearest hotspot and LLVP for the six algorithmically-derived $\mathrm{S_{diff}}$-ULVZs locations and 10,000 randomly placed sets of six ULVZs are shown in Figure S4. The six $\mathrm{S_{diff}}$-ULVZs are seen to significantly correlate with both hotspots and LLVP edges, with more anomalous average distances compared to 97.97% and 99.96% of randomly placed sets of ULVZs, respectively.

In addition to the hotspot database compiled in Steinberger (2000), equivalent analyses were conducted for the databases of Morgan and Morgan (2007) and S. W. French and Romanowicz (2015) (Figure S5). The database of Morgan and Morgan (2007) is based on surface hotspot tracks, while S. W. French and Romanowicz (2015) visually inspect the tomographic model SEMUCB-WM1 (S. French & Romanowicz, 2014) for plumes which are vertically continuous to the CMB. Despite the variety of methods of collation, the trend observed is similar in all.

In the analyses of the distribution of positive and negative picks (Figures S6 and S7), both databases give slightly more significant peaks close to hotspots than Steinberger (2000), but all show similar trends with distance.

An equivalent of the analysis of the locations of the six ULVZs found with the location-determining algorithm is shown in Figure S8. The database from Morgan and Morgan (2007) produces a less significant result than Steinberger (2000) as 13% of randomly placed ULVZ sets have a smaller mean distance. However, the database of S. W. French and Romanowicz (2015) produces a much more significant result than Steinberger (2000) as only 0.5% of randomly placed ULVZ sets have a smaller mean distance. In both cases, the mean distance of the observed ULVZs is similar, but because of the larger number of widely spread hotspots in the database of Morgan and Morgan (2007), the distribution skews towards a lower average distance. In contrast, the limited number of deep-rooted plumes in the dataset of S. W. French and Romanowicz (2015) produce a wider spread of average distances. This reinforces the findings that not all hotspots appear to lie above

ULVZs, and those that do show evidence of being deep-rooted in seismic tomographic models.

Primary analyses on relations to LLVP edges were conducted on the clustering vote map of Cottaar and Lekic (2016), but we also conducted equivalent tests using LLVP edges derived directly from recent global tomographic models based on full-waveform inversion: REVEAL (Thrastarson et al., 2024) and GLAD-M35 (Cui et al., 2024). In both cases, we define LLVP edges as the 1% horizontal shear velocity reduction contour at 2800 km depth (Figure S9).

In the analysis of the distribution of positive and negative picks (Figures S10 and S11), both tomographic models argue for S_{diff}-ULVZs being overrepresented a few degrees within LLVP edges as opposed to directly along LLVP edges. Where exactly the peak lies depends on the shear velocity reduction contour chosen to represent the LLVP edge. If a more extreme velocity reduction was chosen, LLVP edges would move towards their centres and S_{diff}-ULVZs would move outwards relatively. Nevertheless, there is still a significant peak close to LLVP edges, as seen in the case of LLVP edges being defined by the clustering analysis of Cottaar and Lekic (2016).

An equivalent of the analysis of the locations of the ULVZs found with the location-determining algorithm is shown in Figure S12. Both cases produce similar results as with edges defined by the vote cluster map of Cottaar and Lekic (2016). Only 0.03% and 0.12% of randomly placed sets are closer to LLVP edges defined by GLAD-M35 and REVEAL on average than the set of six algorithmically-located S_{diff}-ULVZs.

The maps shown in Figures 5, 6, and 9 exclude postcursors picked and labelled with the lowest confidence level as these were deemed too low quality to include. When included (Figure S13), additional regions of positive detections are observed beneath Nova Scotia, East Africa, the Mediterranean, and the Central Indian Ocean. Sporadic positive detections are seen more widely when looking at only the lowest-confidence positive picks (Figure S14f).

Text S3 — Networks used in this study

The waveform data used in this study are from the following networks: 1A (`https://doi.org/10.7914/SN/1A_2019`, `https://doi.org/10.7914/SN/1A_2007`, `https://doi.org/10.15778/RESIF.1A2009`), 1B, 1C (`https://doi.org/10.7914/SN/1C_2011`), 1D (`https://doi.org/10.7914/SN/1D_2010`, `https://doi.org/10.7914/SN/1D_2016`), 1E (`https://doi.org/10.15778/RESIF.1E2008`), 1F (`https://doi.org/10.7914/SN/1F_2015`), 1G (`https://doi.org/10.7914/SN/1G_2010`), 1J, 1M, 1N (`https://doi.org/10.15778/RESIF.1N2015`), 1P (`https://doi.org/10.7914/SN/1P_2018`), 1Q (`https://doi.org/10.7914/SN/1Q_2019`), 1T (`https://doi.org/10.7914/SN/1T_2015`), 1U (`https://doi.org/10.7914/SN/1U_2013`), 1V, 1Y, 2A (`https://doi.org/10.7914/SN/2A_2017`, `https://doi.org/10.12686/sed/networks/2a`), 2B (`https://doi.org/10.7914/SN/2B_2019`, `https://doi.org/10.7914/SN/2B_2016`), 2C (`https://doi.org/10.7914/SN/2C_2010`, `https://doi.org/10.12686/sed/networks/2c`), 2D, 2E, 2F (`https://doi.org/10.7914/SN/2F_2017`, `https://doi.org/10.7914/SN/2F_2009`), 2G (`https://doi.org/10.7914/SN/2G_2010`), 2H (`https://doi.org/10.7914/SN/2H_2009`, `https://doi.org/10.7914/SN/2H_2016`), 2J, 2K (`https://doi.org/10.7914/SN/2K_2014`), 2L (`https://doi.org/10.7914/SN/2L_2020`), 2M (`https://doi.org/10.7914/SN/2M_2015`), 2O (`https://doi.org/10.7914/SN/2O_2019`), 2P (`https://doi.org/10.7914/SN/2P_2017`), 2S, 2T (`https://doi.org/10.7914/SN/2T`

_2018), 3A (https://doi.org/10.15778/RESIF.3A2008, https://doi.org/10.7914/SN/3A_2021), 3B (https://doi.org/10.7914/SN/3B_2021), 3C (https://doi.org/10.7914/SN/3C_2022, https://doi.org/10.15778/RESIF.3C2019, https://doi.org/10.7914/SN/3C_2017, https://doi.org/10.7914/SN/3C_2014), 3D (https://doi.org/10.7914/SN/3D_2010), 3E (https://doi.org/10.7914/SN/3E_2010), 3H, 3J (https://doi.org/10.7914/SN/3J_2016), 3K (https://doi.org/10.7914/SN/3K_2016), 3L (https://doi.org/10.7914/SN/3L_2010), 3S, 4A (https://doi.org/10.7914/SN/4A_2022, https://doi.org/10.7914/SN/4A_2010, https://doi.org/10.7914/SN/4A_2016), 4B, 4C, 4E (https://doi.org/10.7914/SN/4E_2010), 4F (https://doi.org/10.7914/SN/4F_2007), 4G (https://doi.org/10.15778/RESIF.4G2007), 4H (https://doi.org/10.7914/SN/4H_2011), 4K, 4N, 4O, 4P (https://doi.org/10.7914/SN/4P_2020), 4Q, 4S (https://doi.org/10.7914/SN/4S_2018), 4T (https://doi.org/10.7914/SN/4T_2018), 5A (https://doi.org/10.7914/SN/5A_2005, https://doi.org/10.7914/SN/5A_2010, https://doi.org/10.7914/SN/5A_2014), 5C (https://doi.org/10.7914/SN/5C_2009), 5E, 5F (https://doi.org/10.7914/SN/5F_2015), 5G (https://doi.org/10.7914/SN/5G_2004), 5H (https://doi.org/10.7914/SN/5H_2017, https://doi.org/10.7914/SN/5H_2011, https://doi.org/10.7914/SN/5H_2013), 5J (https://doi.org/10.7914/SN/5J_2014), 5K, 5L, 5M, 5P (https://doi.org/10.7914/SN/5P_2013), 5T, 6A (https://doi.org/10.7914/SN/6A_2017), 6C (https://doi.org/10.7914/SN/6C_2011), 6D (https://doi.org/10.7914/SN/6D_2009), 6E (https://doi.org/10.7914/SN/6E_2013), 6F (https://doi.org/10.7914/SN/6F_2012), 6G (https://doi.org/10.7914/SN/6G_2013), 6H (https://doi.org/10.7914/SN/6H_2022, https://doi.org/10.7914/SN/6H_2011), 6J (https://doi.org/

10.7914/SN/6J_2021), 6K (https://doi.org/10.7914/SN/6K_2014), 6O (https://doi.org/10.7914/SN/6O_2016), 7A (https://doi.org/10.7914/SN/7A_2013), 7B (https://doi.org/10.7914/SN/7B_1993), 7C (https://doi.org/10.15778/RESIF.7C2009, https://doi.org/10.7914/SN/7C_2015), 7D (https://doi.org/10.7914/SN/7D_2011, https://doi.org/10.7914/SN/7D_2009, https://doi.org/10.7914/SN/7D_2022, https://doi.org/10.7914/SN/7D_1997, https://doi.org/10.7914/SN/7D_2018), 7E (https://doi.org/10.7914/SN/7E_1998), 7F, 7G (https://doi.org/10.7914/SN/7G_2014, https://doi.org/10.7914/SN/7G_2021), 7J (https://doi.org/10.7914/SN/7J_2013, https://doi.org/10.7914/SN/7J_2011), 7L, 7M, 7O (https://doi.org/10.7914/SN/7O_2018), 7S, 8A (https://doi.org/10.7914/SN/8A_2015, https://doi.org/10.7914/SN/8A_2008), 8B (https://doi.org/10.7914/SN/8B_2008), 8C (https://doi.org/10.15778/RESIF.8C2019), 8D (https://doi.org/10.12686/sed/networks/8d), 8E (https://doi.org/10.7914/SN/8E_2021), 8F, 8G (https://doi.org/10.7914/SN/8G_2016, https://doi.org/10.7914/SN/8G_2018, https://doi.org/10.7914/SN/8G_2013), 8H, 8P, 8U, 8X (https://doi.org/10.12686/alparray/8x_2016), 9A, 9C (https://doi.org/10.7914/SN/9C_2014), 9D (https://doi.org/10.7914/SN/9D_2010), 9E (https://doi.org/10.12686/sed/networks/9e), 9F (https://doi.org/10.7914/SN/9F_2008), 9G (https://doi.org/10.7914/SN/9G_2016), 9H, 9J, 9K, 9M (https://doi.org/10.7914/SN/9M_2019), 9N, 9P, 9S, A2 (https://doi.org/10.7914/SN/A2), A7, AB, AC (https://doi.org/10.7914/SN/AC), AE (https://doi.org/10.7914/SN/AE), AF (https://doi.org/10.7914/SN/AF), AG, AI (https://doi.org/10.7914/SN/AI), AK (https://doi.org/10.7914/SN/AK), AO, AR, AT (https://doi.org/10.7914/SN/AT), AU, AV (https://doi.org/10.7914/SN/AV), AW, AY, AZ (https://doi.org/

10.7914/SN/AZ), BA, BC (https://doi.org/10.7914/SN/BC), BE (https://doi.org/10.7914/SN/BE), BK, BL, BN, BQ (https://doi.org/10.7914/SN/BQ), BR, BS (https://doi.org/10.7914/SN/BS), BW (https://doi.org/10.7914/SN/BW), BX (https://doi.org/10.7914/SN/BX), C, C0 (https://doi.org/10.7914/SN/C0), C1 (https://doi.org/10.7914/SN/C1), C4 (https://doi.org/10.12686/sed/networks/c4), C8, CA (https://doi.org/10.7914/SN/CA), CB (https://doi.org/10.7914/SN/CB), CC (https://doi.org/10.7914/SN/CC), CD (https://doi.org/10.7914/SN/CD), CH (https://doi.org/10.12686/sed/networks/ch), CI (https://doi.org/10.7914/SN/CI), CK, CL (https://doi.org/10.15778/RESIF.CL), CM (https://doi.org/10.7914/SN/CM), CN (https://doi.org/10.7914/SN/CN), CO (https://doi.org/10.7914/SN/CO), CP, CQ (https://doi.org/10.7914/SN/CQ), CR (https://doi.org/10.7914/SN/CR), CT, CU (https://doi.org/10.7914/SN/CU), CW (https://doi.org/10.7914/SN/CW), CX, CY, CZ (https://doi.org/10.7914/SN/CZ), DE, DK, DR (https://doi.org/10.7914/SN/DR), DU (https://doi.org/10.7914/SN/DU), DZ, EB (https://doi.org/10.7914/SN/EB), EC, EE, EI (https://doi.org/10.7914/SN/EI), EO (https://doi.org/10.7914/SN/EO), EP, ER, ES (https://doi.org/10.7914/SN/ES), ET, FN, FO, FR (https://doi.org/10.15778/RESIF.FR), G, G2 (https://doi.org/10.12686/SED/NETWORKS/G2), GB, GE, GG (https://doi.org/10.7914/SN/GG), GH (https://doi.org/10.7914/SN/GH), GI (https://doi.org/10.7914/SN/GI), GL, GM (https://doi.org/10.7914/SN/GM), GO, GQ, GR, GS (https://doi.org/10.7914/SN/GS), GT (https://doi.org/10.7914/SN/GT), GU (https://doi.org/10.7914/SN/GU), GX, H2, HA (https://doi.org/10.7914/SN/HA), HC (https://doi.org/10.7914/SN/HC), HE, HF, HK, HL (https://doi.org/10.7914/

SN/HL), HP (`https://doi.org/10.7914/SN/HP`), HS (`https://doi.org/10.7914/SN/HS`), HT (`https://doi.org/10.7914/SN/HT`), HU, HV (`https://doi.org/10.7914/SN/HV`), HW, IB (`https://doi.org/10.7914/SN/IB`), IC (`https://doi.org/10.7914/SN/IC`), IE (`https://doi.org/10.7914/SN/IE`), II (`https://doi.org/10.7914/SN/II`), IJ (`https://doi.org/10.7914/SN/IJ`), IM, IN, IO (`https://doi.org/10.7914/SN/IO`), IP, IQ, IS, IU (`https://doi.org/10.7914/SN/IU`), IV, IW (`https://doi.org/10.7914/SN/IW`), IX, IY (`https://doi.org/10.7914/SN/IY`), JM, JP, JS, K5 (`https://doi.org/10.7914/SN/K5`), KC (`https://doi.org/10.7914/SN/KC`), KG, KN (`https://doi.org/10.7914/SN/KN`), KO (`https://doi.org/10.7914/SN/KO`), KP (`https://doi.org/10.7914/SN/KP`), KQ (`https://doi.org/10.7914/SN/KQ`), KR (`https://doi.org/10.7914/SN/KR`), KS, KV, KW, KY (`https://doi.org/10.7914/SN/KY`), KZ (`https://doi.org/10.7914/SN/KZ`), LB, LC (`https://doi.org/10.7914/SN/LC`), LD (`https://doi.org/10.7914/SN/LD`), LE (`https://doi.org/10.7914/SN/LE`), LI (`https://doi.org/10.7914/SN/LI`), LM (`https://doi.org/10.7914/SN/LM`), LX (`https://doi.org/10.7914/SN/LX`), MB (`https://doi.org/10.7914/SN/MB`), MC, MD (`https://doi.org/10.7914/SN/MD`), ME (`https://doi.org/10.7914/SN/ME`), MG (`https://doi.org/10.7914/SN/MG`), MI (`https://doi.org/10.7914/SN/MI`), MK, ML (`https://doi.org/10.7914/SN/ML`), MM (`https://doi.org/10.7914/SN/MM`), MN, MP (`https://doi.org/10.7914/SN/MP`), MQ, MR, MS, MT (`https://doi.org/10.15778/RESIF.MT`), MU, MX (`https://doi.org/10.21766/SSNMX/SN/MX`), MY, MZ, N4 (`https://doi.org/10.7914/SN/N4`), NA, ND (`https://doi.org/10.15778/RESIF.ND`), NE (`https://doi.org/10.7914/SN/NE`), NI (`https://doi.org/10.7914/SN/NI`), NJ (`https://doi.org/10.7914/SN/NJ`), NK (`https://doi.org/10.7914/SN/NK`), NL, NM, NN (`https://doi`

.org/10.7914/SN/NN), NO, NR (https://doi.org/10.7914/SN/NR), NU (https://doi.org/10.7914/SN/NU), NV (https://doi.org/10.7914/SN/NV), NW, NX (https://doi.org/10.7914/SN/NX), NY (https://doi.org/10.7914/SN/NY), NZ, O2 (https://doi.org/10.7914/SN/O2), OC, OE (https://doi.org/10.7914/SN/OE), OH (https://doi.org/10.7914/SN/OH), OI, OK (https://doi.org/10.7914/SN/OK), ON (https://doi.org/10.7914/SN/ON), OO (https://doi.org/10.7914/SN/OO), OR (https://doi.org/10.7914/SN/OR), OT (https://doi.org/10.7914/SN/OT), OV (https://doi.org/10.7914/SN/OV), OX (https://doi.org/10.7914/SN/OX), PA (https://doi.org/10.7914/SN/PA), PB, PE (https://doi.org/10.7914/SN/PE), PF, PG, PL, PM (https://doi.org/10.7914/SN/PM), PN, PO, PQ (https://doi.org/10.7914/SN/PQ), PR (https://doi.org/10.7914/SN/PR), PS, PT (https://doi.org/10.7914/SN/PT), PY (https://doi.org/10.7914/SN/PY), QM, QZ (https://doi.org/10.7914/SN/QZ), RC (https://doi.org/10.7914/SN/RC), RD (https://doi.org/10.15778/RESIF.RD), RE, RF (https://doi.org/10.7914/SN/RF), RI, RM (https://doi.org/10.7914/SN/RM), RN (https://doi.org/10.7914/SN/RN), RO (https://doi.org/10.7914/SN/RO), RV (https://doi.org/10.7914/SN/RV), S1 (https://doi.org/10.7914/SN/S1), S8, SB (https://doi.org/10.7914/SN/SB), SC, SF, SI, SJ (https://doi.org/10.7914/SN/SJ), SK, SL (https://doi.org/10.7914/SN/SL), SN (https://doi.org/10.7914/SN/SN), SP (https://doi.org/10.7914/SN/SP), SS (https://doi.org/10.7914/SN/SS), ST (https://doi.org/10.7914/SN/ST), SV, SX (https://doi.org/10.7914/SN/SX), TA (https://doi.org/10.7914/SN/TA), TC (https://doi.org/10.15517/TC), TD, TH (https://doi.org/10.7914/SN/TH), TJ (https://doi.org/10.7914/SN/TJ), TM, TO, TQ, TR, TT, TU (https://doi.org/10.7914/SN/TU), TV, TW (https://doi.org/10.7914/SN/TW), TX (https://doi.org/10.7914/SN/TX), TZ (https://doi.org/10.7914/SN/TZ), UD (https://doi.org/10.7914/SN/UD), UI, UK, UM (https://doi.org/10.7914/SN/UM), UO (https://doi.org/10.7914/SN/UO), UP, US (https://doi.org/10.7914/SN/US), UU (https://doi.org/10.7914/SN/UU), UW (https://doi.org/10.7914/SN/UW), VI, VM, VU, WA, WC, WI, WM, WR, WU, WW (https://doi.org/10.7914/SN/WW), WY (https://doi.org/10.7914/SN/WY), X1, X2 (https://doi.org/10.7914/SN/X2_2005), X3 (https://doi.org/10.7914/SN/X3_2007, https://doi.org/10.7914/SN/X3_2018, https://doi.org/10.7914/SN/X3_2015), X4 (https://doi.org/10.7914/SN/X4_2007, https://doi.org/10.7914/SN/X4_2010, https://doi.org/10.7914/SN/X4_2016), X5, X6 (https://doi.org/10.7914/SN/X6_2007, https://doi.org/10.7914/SN/X6_2014), X7 (https://doi.org/10.7914/SN/X7_2016, https://doi.org/10.15778/RESIF.X72010), X8 (https://doi.org/10.7914/SN/X8_2012), X9 (https://doi.org/10.7914/SN/X9_2008, https://doi.org/10.7914/SN/X9_2004, https://doi.org/10.7914/SN/X9_2012), XA (https://doi.org/10.7914/SN/XA_1995, https://doi.org/10.7914/SN/XA_2017, https://doi.org/10.12686/sed/networks/xa, https://doi.org/10.7914/SN/XA_2008, https://doi.org/10.7914/SN/XA_2002, https://doi.org/10.7914/SN/XA_1997), XB (https://doi.org/10.7914/SN/XB_2000, https://doi.org/10.7914/SN/XB_2005, https://doi.org/10.7914/SN/XB_2009, https://doi.org/10.7914/SN/XB_2003, https://doi.org/10.7914/SN/XB_1993, https://doi.org/10.7914/SN/XB_1997, https://doi.org/10.7914/SN/XB_2014), XC (https://doi.org/10.7914/SN/XC_2006, https://doi.org/10.7914/SN/XC_2011, https://doi.org/10.7914/SN/XC_2000, https://doi.org/10.7914/SN/XC_2012, https://doi.org/10.7914/SN/XC_1995), XD (https://doi.org/10.7914/

SN/XD_1994, https://doi.org/10.7914/SN/XD_2002, https://doi.org/10.7914/SN/XD_2014, https://doi.org/10.7914/SN/XD_1999, https://doi.org/10.7914/SN/XD_2007, https://doi.org/10.7914/SN/XD_2011, https://doi.org/10.7914/SN/XD_2001), XE (https://doi.org/10.7914/SN/XE_1994, https://doi.org/10.7914/SN/XE_2005, https://doi.org/10.7914/SN/XE_1999, https://doi.org/10.7914/SN/XE_2009, https://doi.org/10.7914/SN/XE_1996, https://doi.org/10.7914/SN/XE_2003), XF (https://doi.org/10.7914/SN/XF_2021, https://doi.org/10.7914/SN/XF_2006, https://doi.org/10.7914/SN/XF_2014, https://doi.org/10.7914/SN/XF_2012, https://doi.org/10.7914/SN/XF_2002, https://doi.org/10.7914/SN/XF_2000, https://doi.org/10.7914/SN/XF_2009), XG (https://doi.org/10.7914/SN/XG_2002, https://doi.org/10.7914/SN/XG_1999), XH (https://doi.org/10.7914/SN/XH_2002, https://doi.org/10.7914/SN/XH_2004, https://doi.org/10.12686/sed/networks/xh, https://doi.org/10.7914/SN/XH_2007, https://doi.org/10.7914/SN/XH_2012, https://doi.org/10.7914/SN/XH_1996, https://doi.org/10.7914/SN/XH_2008, https://doi.org/10.7914/SN/XH_1994, https://doi.org/10.7914/SN/XH_2014), XI (https://doi.org/10.7914/SN/XI_2011, https://doi.org/10.7914/SN/XI_2007, https://doi.org/10.7914/SN/XI_2014, https://doi.org/10.7914/SN/XI_2018, https://doi.org/10.7914/SN/XI_1995, https://doi.org/10.7914/SN/XI_1998, https://doi.org/10.7914/SN/XI_2000), XJ (https://doi.org/10.7914/SN/XJ_2010, https://doi.org/10.7914/SN/XJ_2008, https://doi.org/10.7914/SN/XJ_1997, https://doi.org/10.15778/RESIF.XJ2009, https://doi.org/10.7914/SN/XJ_1998, https://doi.org/10.7914/SN/XJ_1995, https://doi.org/10.7914/SN/XJ_2000, https://doi.org/10.7914/SN/XJ_2012, https://doi.org/10.7914/SN/XJ_2013), XK (https://doi.org/10.7914/

SN/XK_1998, https://doi.org/10.7914/SN/XK_2012, https://doi.org/10.7914/SN/XK_1999, https://doi.org/10.7914/SN/XK_2004, https://doi.org/10.7914/SN/XK_1997, https://doi.org/10.7914/SN/XK_2001, https://doi.org/10.15778/RESIF.XK2007), XL (https://doi.org/10.7914/SN/XL_2012, https://doi.org/10.7914/SN/XL_2008, https://doi.org/10.7914/SN/XL_1997), XM (https://doi.org/10.7914/SN/XM_1998, https://doi.org/10.7914/SN/XM_2012, https://doi.org/10.7914/SN/XM_1995, https://doi.org/10.7914/SN/XM_2022, https://doi.org/10.7914/SN/XM_1999, https://doi.org/10.7914/SN/XM_2011), XN (https://doi.org/10.7914/SN/XN_2000, https://doi.org/10.7914/SN/XN_2003, https://doi.org/10.7914/SN/XN_2008, https://doi.org/10.7914/SN/XN_2010, https://doi.org/10.7914/SN/XN_1998), XO (https://doi.org/10.7914/SN/XO_2003, https://doi.org/10.7914/SN/XO_2011, https://doi.org/10.7914/SN/XO_2018, https://doi.org/10.7914/SN/XO_1997), XP (https://doi.org/10.7914/SN/XP_2000, https://doi.org/10.7914/SN/XP_2010, https://doi.org/10.15778/RESIF.XP2023, https://doi.org/10.7914/SN/XP_2020, https://doi.org/10.7914/SN/XP_2022, https://doi.org/10.7914/SN/XP_2005, https://doi.org/10.7914/SN/XP_1994, https://doi.org/10.7914/SN/XP_2008, https://doi.org/10.7914/SN/XP_2015, https://doi.org/10.12686/SED/NETWORKS/XP), XQ (https://doi.org/10.7914/SN/XQ_1999, https://doi.org/10.7914/SN/XQ_2011, https://doi.org/10.7914/SN/XQ_2007, https://doi.org/10.7914/SN/XQ_2019, https://doi.org/10.7914/SN/XQ_2012, https://doi.org/10.7914/SN/XQ_2001), XR (https://doi.org/10.7914/SN/XR_2008, https://doi.org/10.7914/SN/XR_2018, https://doi.org/10.7914/SN/XR_2004, https://doi.org/10.7914/SN/XR_2012, https://doi.org/10.7914/SN/XR_2016, https://doi.org/10.7914/SN/XR_1997, https://doi

.org/10.7914/SN/XR_2001), XS (https://doi.org/10.7914/SN/XS_2018, https://doi.org/10.7914/SN/XS_2002, https://doi.org/10.15778/RESIF.XS2010, https://doi.org/10.7914/SN/XS_1999, https://doi.org/10.7914/SN/XS_2006), XT (https://doi.org/10.7914/SN/XT_2011, https://doi.org/10.7914/SN/XT_2003, https://doi.org/10.12686/alparray/xt_2014, https://doi.org/10.15778/RESIF.XT2018, https://doi.org/10.7914/SN/XT_2001, https://doi.org/10.7914/SN/XT_1997, https://doi.org/10.7914/SN/XT_1994, https://doi.org/10.7914/SN/XT_2009), XU (https://doi.org/10.7914/SN/XU_2016, https://doi.org/10.7914/SN/XU_1996, https://doi.org/10.7914/SN/XU_2006), XV (https://doi.org/10.7914/SN/XV_2003, https://doi.org/10.7914/SN/XV_2011, https://doi.org/10.7914/SN/XV_2009, https://doi.org/10.7914/SN/XV_2014), XW (https://doi.org/10.15778/RESIF.XW2007, https://doi.org/10.7914/SN/XW_1997, https://doi.org/10.7914/SN/XW_2012, https://doi.org/10.7914/SN/XW_2009, https://doi.org/10.7914/SN/XW_2017), XX (https://doi.org/10.7914/SN/XX_2013), XY (https://doi.org/10.7914/SN/XY_2010, https://doi.org/10.15778/RESIF.XY2007, https://doi.org/10.7914/SN/XY_1999, https://doi.org/10.7914/SN/XY_2011, https://doi.org/10.7914/SN/XY_1997, https://doi.org/10.7914/SN/XY_2005), XZ (https://doi.org/10.7914/SN/XZ_2005, https://doi.org/10.7914/SN/XZ_2003, https://doi.org/10.7914/SN/XZ_1999), Y1 (https://doi.org/10.7914/SN/Y1_2018), Y2 (https://doi.org/10.7914/SN/Y2_2015, https://doi.org/10.7914/SN/Y2_2013, https://doi.org/10.15778/RESIF.Y22014, https://doi.org/10.7914/SN/Y2_2007), Y3 (https://doi.org/10.7914/SN/Y3_2008, https://doi.org/10.7914/SN/Y3_2009, https://doi.org/10.7914/SN/Y3_2017, https://doi.org/10.7914/SN/Y3_2007), Y4 (https://doi.org/10.15778/RESIF.Y42004, https://

doi.org/10.7914/SN/Y4_2020), Y5 (https://doi.org/10.12686/SED/NETWORKS/Y5), Y6 (https://doi.org/10.7914/SN/Y6_2016, https://doi.org/10.7914/SN/Y6_2006), Y7 (https://doi.org/10.7914/SN/Y7_2009), Y8 (https://doi.org/10.7914/SN/Y8_2009), Y9 (https://doi.org/10.15778/RESIF.Y92009, https://doi.org/10.7914/SN/Y9_2016), YA (https://doi.org/10.7914/SN/YA_2003, https://doi.org/10.7914/SN/YA_2012, https://doi.org/10.15778/RESIF.YA2009, https://doi.org/10.7914/SN/YA_2017, https://doi.org/10.7914/SN/YA_1998), YB (https://doi.org/10.15778/RESIF.YB2010, https://doi.org/10.7914/SN/YB_1998, https://doi.org/10.7914/SN/YB_2018, https://doi.org/10.7914/SN/YB_2005, https://doi.org/10.15778/RESIF.YB2000, https://doi.org/10.7914/SN/YB_2003, https://doi.org/10.7914/SN/YB_2013, https://doi.org/10.7914/SN/YB_1996, https://doi.org/10.7914/SN/YB_2004, https://doi.org/10.7914/SN/YB_2008), YC (https://doi.org/10.7914/SN/YC_2000, https://doi.org/10.7914/SN/YC_2006, https://doi.org/10.7914/SN/YC_2018, https://doi.org/10.7914/SN/YC_2011, https://doi.org/10.7914/SN/YC_2003, https://doi.org/10.7914/SN/YC_2022), YD (https://doi.org/10.7914/SN/YD_2003, https://doi.org/10.7914/SN/YD_2007, https://doi.org/10.7914/SN/YD_2019), YE (https://doi.org/10.7914/SN/YE_2011), YF (https://doi.org/10.7914/SN/YF_1999, https://doi.org/10.7914/SN/YF_2012, https://doi.org/10.7914/SN/YF_2003), YG (https://doi.org/10.7914/SN/YG_2016, https://doi.org/10.7914/SN/YG_2020), YH (https://doi.org/10.7914/SN/YH_2004, https://doi.org/10.7914/SN/YH_2016, https://doi.org/10.7914/SN/YH_2010, https://doi.org/10.7914/SN/YH_2008, https://doi.org/10.7914/SN/YH_2012, https://doi.org/10.7914/SN/YH_2014), YI (https://doi.org/10.7914/SN/YI_1997, https://doi.org/

10.7914/SN/YI_2010, https://doi.org/10.15778/RESIF.YI2015, https://doi.org/10.15778/RESIF.YI2008, https://doi.org/10.7914/SN/YI_2003), YJ (https://doi.org/10.7914/SN/YJ_2004, https://doi.org/10.7914/SN/YJ_1999), YK (https://doi.org/10.7914/SN/YK_2019, https://doi.org/10.7914/SN/YK_2003), YL (https://doi.org/10.7914/SN/YL_2005, https://doi.org/10.7914/SN/YL_2021, https://doi.org/10.7914/SN/YL_2013, https://doi.org/10.7914/SN/YL_2001, https://doi.org/10.7914/SN/YL_2012), YM (https://doi.org/10.7914/SN/YM_2002, https://doi.org/10.7914/SN/YM_2004, https://doi.org/10.7914/SN/YM_2006, https://doi.org/10.7914/SN/YM_2010, https://doi.org/10.7914/SN/YM_2013), YN (https://doi.org/10.7914/SN/YN_2010, https://doi.org/10.7914/SN/YN_2005), YO (https://doi.org/10.7914/SN/YO_2014, https://doi.org/10.7914/SN/YO_2003, https://doi.org/10.7914/SN/YO_2009, https://doi.org/10.7914/SN/YO_2010), YP (https://doi.org/10.7914/SN/YP_2009, https://doi.org/10.15778/RESIF.YP2012), YQ (https://doi.org/10.7914/SN/YQ_2013, https://doi.org/10.7914/SN/YQ_2009, https://doi.org/10.7914/SN/YQ_2017), YR (https://doi.org/10.7914/SN/YR_2008, https://doi.org/10.7914/SN/YR_2016, https://doi.org/10.15778/RESIF.YR2013, https://doi.org/10.15778/RESIF.YR1999), YS (https://doi.org/10.7914/SN/YS_2009, https://doi.org/10.7914/SN/YS_2014, https://doi.org/10.7914/SN/YS_2001), YT (https://doi.org/10.15778/RESIF.YT2003, https://doi.org/10.15778/RESIF.YT2001, https://doi.org/10.7914/SN/YT_2007), YU (https://doi.org/10.7914/SN/YU_2016, https://doi.org/10.7914/SN/YU_2019, https://doi.org/10.7914/SN/YU_2006), YV (https://doi.org/10.7914/SN/YV_2019, https://doi.org/10.15778/RESIF.YV2011, https://doi.org/10.7914/SN/YV_2006), YW (https://doi.org/10.7914/SN/YW_2007, https://

doi.org/10.7914/SN/YW_2005, https://doi.org/10.7914/SN/YW_2021, https://doi.org/10.15778/RESIF.YW2017), YX (https://doi.org/10.7914/SN/YX_2010, https://doi.org/10.15778/RESIF.YX2001, https://doi.org/10.7914/SN/YX_2016), YY (https://doi.org/10.7914/SN/YY_2012, https://doi.org/10.7914/SN/YY_2000, https://doi.org/10.7914/SN/YY_2013), YZ (https://doi.org/10.7914/SN/YZ_2008, https://doi.org/10.7914/SN/YZ_2009, https://doi.org/10.15778/RESIF.YZ2004), Z1 (https://doi.org/10.7914/SN/Z1_2009, https://doi.org/10.7914/SN/Z1_2006, https://doi.org/10.7914/SN/Z1_2016), Z2, Z3 (https://doi.org/10.12686/alparray/z3_2015), Z4 (https://doi.org/10.7914/SN/Z4_2009, https://doi.org/10.15778/RESIF.Z42023), Z5 (https://doi.org/10.7914/SN/Z5_2013, https://doi.org/10.7914/SN/Z5_2022, https://doi.org/10.7914/SN/Z5_2018), Z6 (https://doi.org/10.7914/SN/Z6_2011), Z7 (https://doi.org/10.7914/SN/Z7_2010, https://doi.org/10.7914/SN/Z7_2019), Z8 (https://doi.org/10.7914/SN/Z8_2006, https://doi.org/10.7914/SN/Z8_2009, https://doi.org/10.7914/SN/Z8_2013), Z9 (https://doi.org/10.7914/SN/Z9_2010, https://doi.org/10.12686/SED/NETWORKS/Z9), ZA (https://doi.org/10.7914/SN/ZA_2006), ZB (https://doi.org/10.7914/SN/ZB_2017), ZC (https://doi.org/10.7914/SN/ZC_2013, https://doi.org/10.7914/SN/ZC_2006), ZD (https://doi.org/10.7914/SN/ZD_2010), ZE (https://doi.org/10.7914/SN/ZE_2007, https://doi.org/10.7914/SN/ZE_2015), ZF (https://doi.org/10.15778/RESIF.ZF2015, https://doi.org/10.15778/RESIF.ZF2003), ZG (https://doi.org/10.7914/SN/ZG_2006, https://doi.org/10.7914/SN/ZG_2010, https://doi.org/10.7914/SN/ZG_2004), ZH (https://doi.org/10.7914/SN/ZH_2004, https://doi.org/10.15778/RESIF.ZH2003, https://doi.org/10.7914/SN/ZH_2011, https://doi.org/10.15778/RESIF.ZH2016), ZI (https://

doi.org/10.7914/SN/ZI_2018, https://doi.org/10.15778/RESIF.ZI2001, https://doi.org/10.7914/SN/ZI_2011), ZJ (https://doi.org/10.7914/SN/ZJ_2012), ZK (https://doi.org/10.7914/SN/ZK_2009), ZL (https://doi.org/10.7914/SN/ZL_2011, https://doi.org/10.7914/SN/ZL_2007), ZM (https://doi.org/10.7914/SN/ZM_2014, https://doi.org/10.7914/SN/ZM_2007), ZN (https://doi.org/10.7914/SN/ZN_2010), ZO (https://doi.org/10.7914/SN/ZO_2019, https://doi.org/10.7914/SN/ZO_2010, https://doi.org/10.15778/RESIF.ZO2008, https://doi.org/10.15778/RESIF.ZO2014), ZP (https://doi.org/10.7914/SN/ZP_2007, https://doi.org/10.7914/SN/ZP_2016), ZQ (https://doi.org/10.7914/SN/ZQ_2015, https://doi.org/10.7914/SN/ZQ_2013, https://doi.org/10.7914/SN/ZQ_2001), ZR (https://doi.org/10.7914/SN/ZR_2015, https://doi.org/10.7914/SN/ZR_2013), ZS (https://doi.org/10.15778/RESIF.ZS2007, https://doi.org/10.7914/SN/ZS_2014), ZT (https://doi.org/10.7914/SN/ZT_2015, https://doi.org/10.7914/SN/ZT_2012), ZU (https://doi.org/10.7914/SN/ZU_2009, https://doi.org/10.15778/RESIF.ZU2015), ZV (https://doi.org/10.7914/SN/ZV_2016, https://doi.org/10.7914/SN/ZV_2014, https://doi.org/10.7914/SN/ZV_2008), ZW (https://doi.org/10.7914/SN/ZW_2007, https://doi.org/10.7914/SN/ZW_2013), ZX (https://doi.org/10.7914/SN/ZX_2011, https://doi.org/10.7914/SN/ZX_2021, https://doi.org/10.7914/SN/ZX_2003), ZY, ZZ (https://doi.org/10.7914/SN/ZZ_2010, https://doi.org/10.7914/SN/ZZ_2012, https://doi.org/10.7914/SN/ZZ_2019).

References

Bailey, H. P. (1956). Two grid systems that divide the entire surface of the Earth into quadrilaterals of equal area. *Eos, Transactions American Geophysical Union*, *37*(5), 628–635.

Cottaar, S., & Lekic, V. (2016). Morphology of seismically slow lower-mantle structures. *Geophysical Supplements to the Monthly Notices of the Royal Astronomical Society*, *207*(2), 1122–1136.

Cui, C., Lei, W., Liu, Q., Peter, D., Bozdağ, E., Tromp, J., ... Pugmire, D. (2024). GLAD-M35: a joint P and S global tomographic model with uncertainty quantification. *Geophysical Journal International*, *239*(1), 478–502.

French, S., & Romanowicz, B. A. (2014). Whole-mantle radially anisotropic shear velocity structure from spectral-element waveform tomography. *Geophysical Journal International*, *199*(3), 1303–1327.

French, S. W., & Romanowicz, B. (2015). Broad plumes rooted at the base of the Earth's mantle beneath major hotspots. *Nature*, *525*(7567), 95–99.

Morgan, W. J., & Morgan, J. P. (2007). Plate velocities in the hotspot reference frame. *Plates, Plumes, and Planetary Processes*, *430*, 65.

Steinberger, B. (2000). Plumes in a convecting mantle: Models and observations for individual hotspots. *Journal of Geophysical Research: Solid Earth*, *105*(B5), 11127–11152.

Thrastarson, S., van Herwaarden, D.-P., Noe, S., Josef Schiller, C., & Fichtner, A. (2024). REVEAL: A global full-waveform inversion model. *Bulletin of the Seismological Society of America*, *114*(3), 1392–1406.

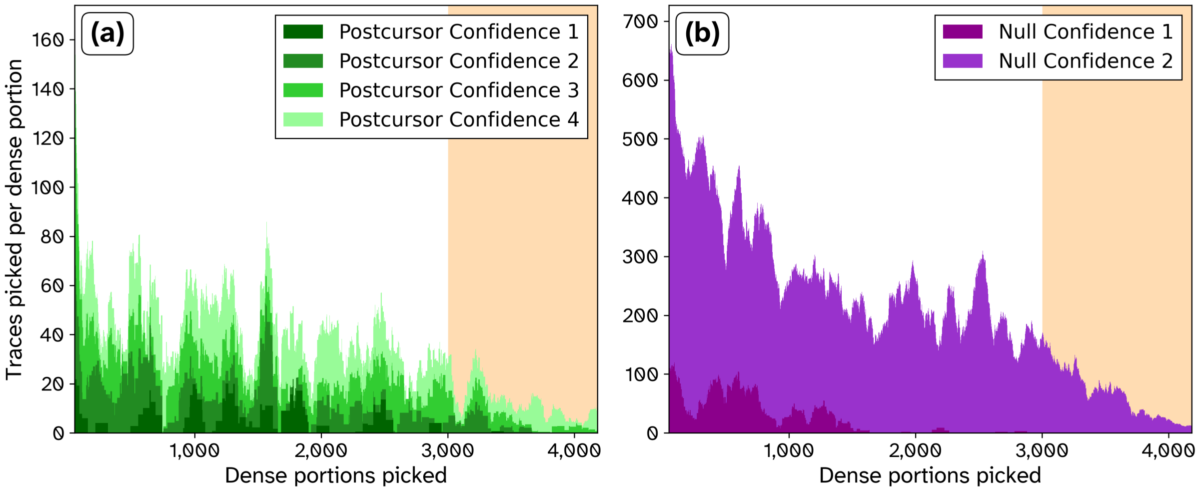

Figure S1. Running average over 100 dense portions of the number of traces picked at each confidence level per dense portion for positive (a) and negative (b) picks. Orange shaded regions show the portion of picking where only uncommon geometries were picked.

Confidence	Number of Azimuth Bins	Number of Traces
Null Confidence 1	5,508	84,542
Null Confidence 2	41,552	836,941
Positive Confidence 1	663	16,392
Positive Confidence 2	1,720	38,588
Positive Confidence 3	2,475	44,491
Positive Confidence 4	3,338	55,341
Low quality	137,150	963,119

Table S1. Total numbers of azimuth bins and traces picked at each null and positive confidence level, as well as azimuth bins picked as too low-quality to use.

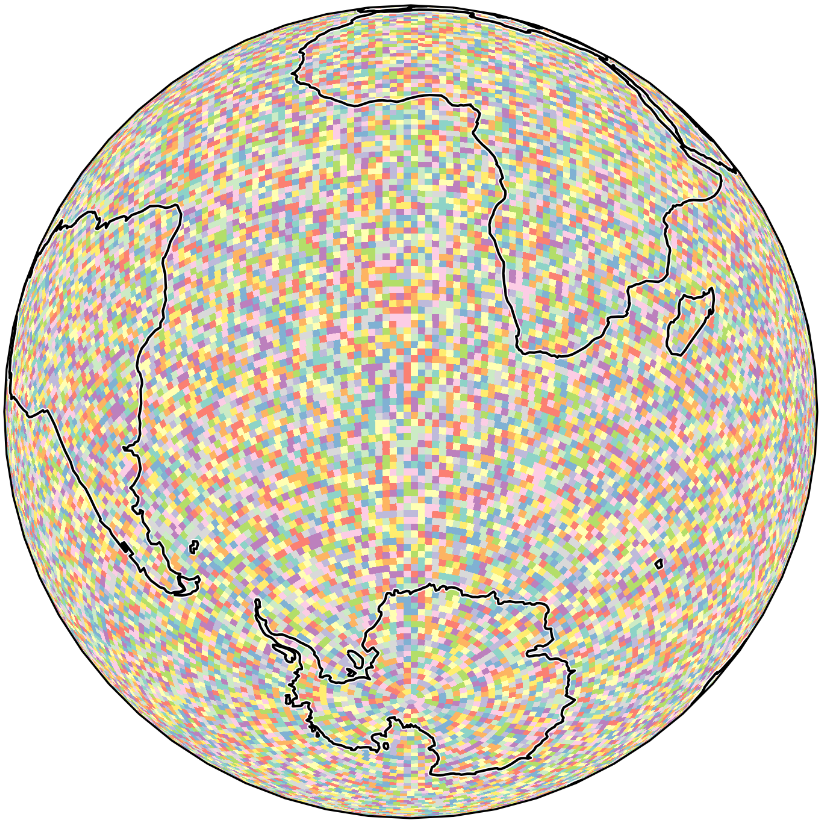

Figure S2. Cells that form the approximately equal-area grid, coloured randomly. Constructed following Bailey (1956).

Order	Latitude	Longitude	Approximate Region
1	18.5	-167.33	Hawaii
2	-10.5	-15.76	St. Helena
3	66.5	-21.25	Iceland
4	9.5	-106.99	Galápagos
5	-29.5	178.85	Vanuatu
6	-33.5	-131.40	Pitcairn

Table S2. Algorithmically-determined locations of the six S_{diff}-ULVZs that explain 99% of positive regions on the differential global map.

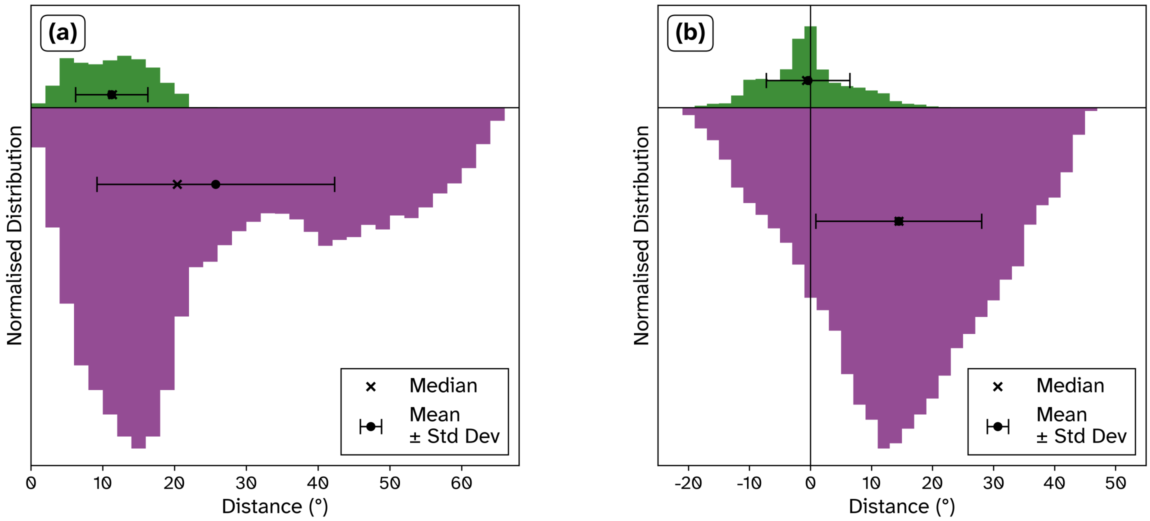

Figure S3. Distance distribution of positive (green) and negative (purple) detections relative to the closest hotspot (a) or LLVP edge (b). The distance distributions are the summed cell counts of the positive and negative portions of the differential map.

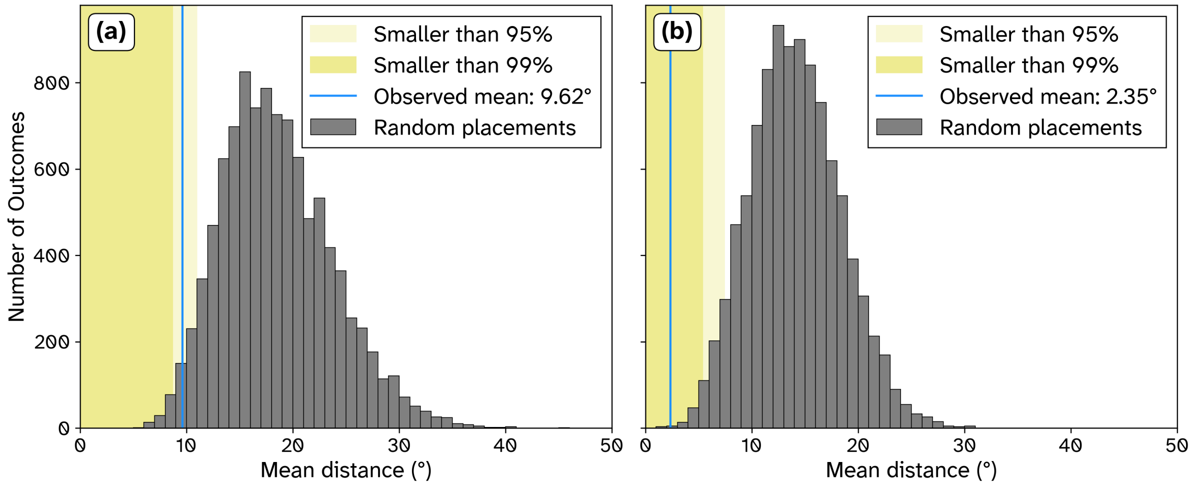

Figure S4. (a) Mean distance between the centre of each ULVZ and the closest hotspot for 10,000 randomly placed sets of ULVZs, binned and shown in grey. The mean distance of the six ULVZs from the location-finding algorithm is shown as a blue line, and values smaller than 95% and 99% of the 10,000 sets are highlighted in lighter and darker shades of yellow respectively. (b) Equivalent plot for LLVP edges.

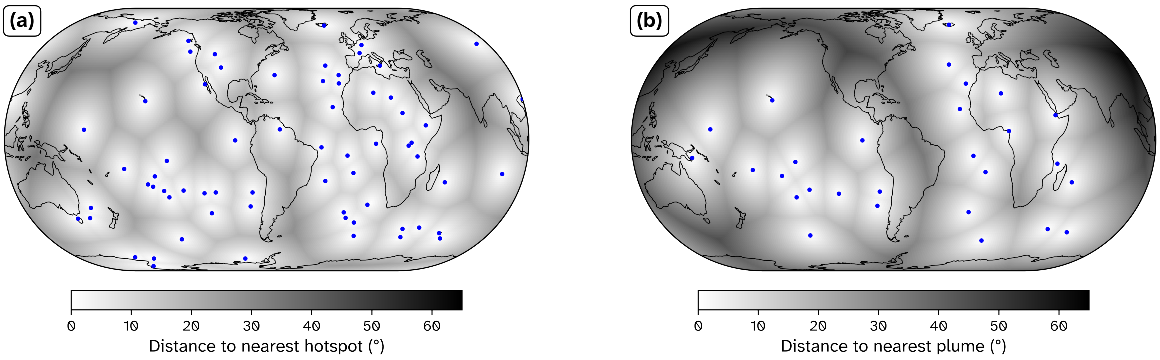

Figure S5. Equivalent of Figure 4a, but using the hotspot databases of Morgan and Morgan (2007) and S. W. French and Romanowicz (2015), shown in (a) and (b) respectively.

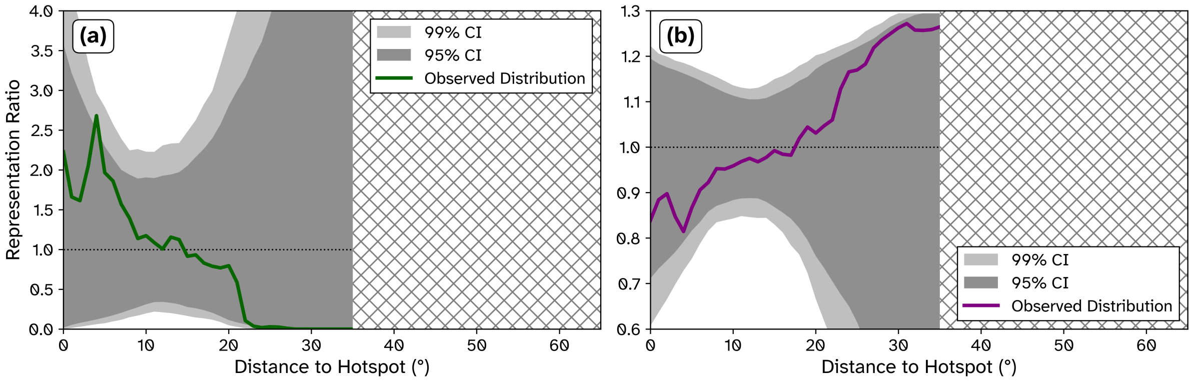

Figure S6. Equivalent of Figure 7, but for the hotspot database of Morgan and Morgan (2007).

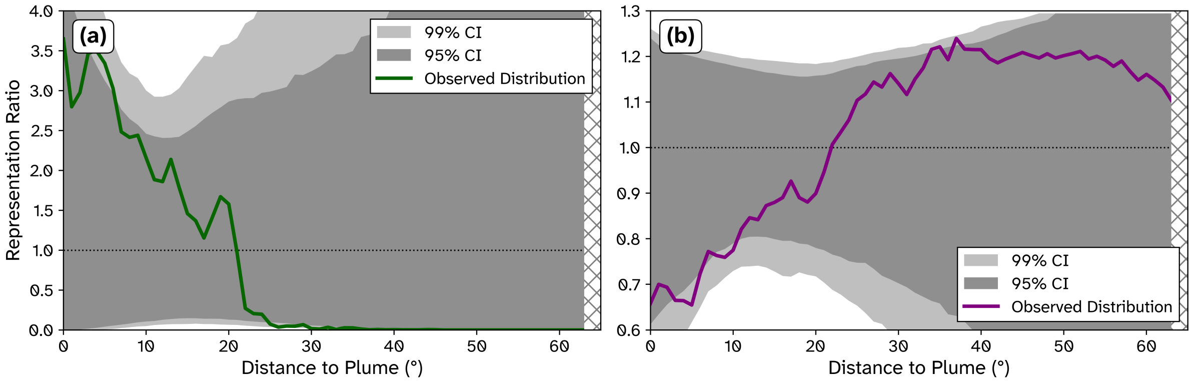

Figure S7. Equivalent of Figure 7, but for the plume database of S. W. French and Romanowicz (2015).

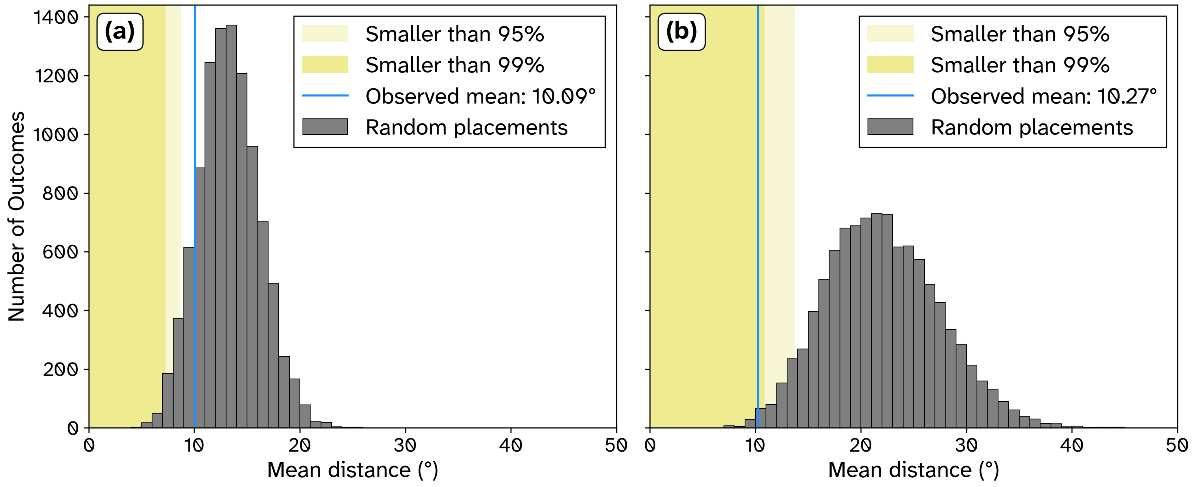

Figure S8. Equivalent of Figure S4a, but using the hotspot databases of Morgan and Morgan (2007) and S. W. French and Romanowicz (2015), shown in (a) and (b) respectively.

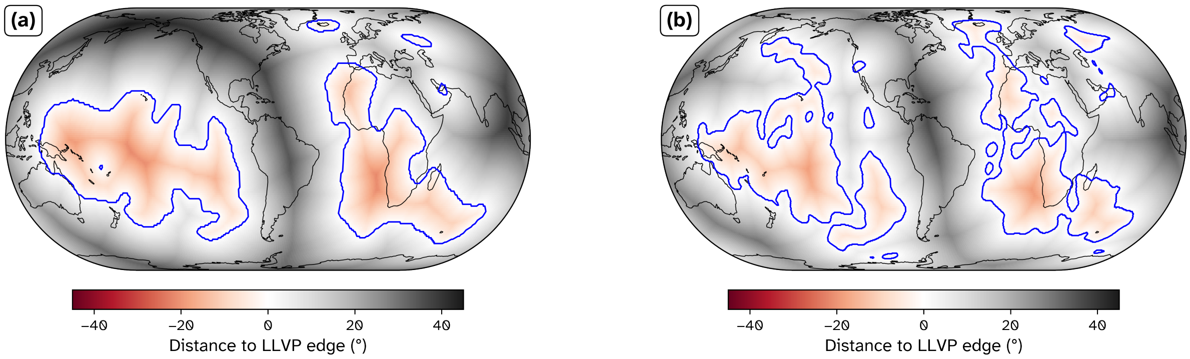

Figure S9. Equivalent of Figure 4b, but with LLVP edges defined by the 1% horizontal shear velocity reduction contour at 2800 km depth in the tomographic models (a) GLAD-M35 (Cui et al., 2024) and (b) REVEAL (Thrastarson et al., 2024).

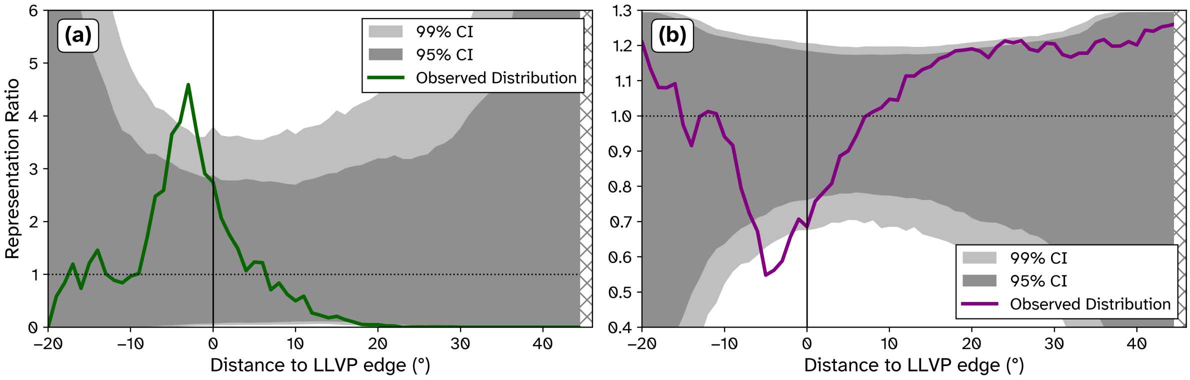

Figure S10. Equivalent of Figure 8, but with LLVP edges defined by the 1% horizontal shear velocity reduction contour at 2800 km depth in the tomographic model GLAD-M35.

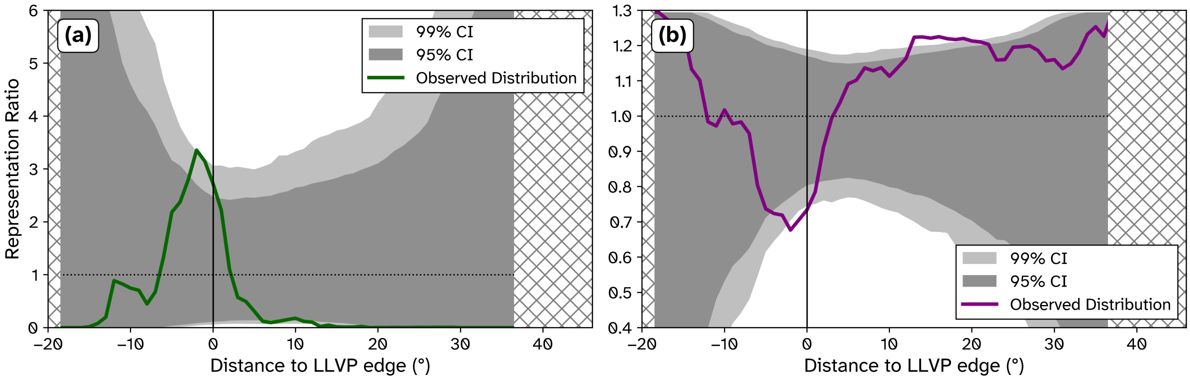

Figure S11. Equivalent of Figure 8 but with LLVP edges defined by the 1% horizontal shear velocity reduction contour at 2800 km depth in the tomographic model REVEAL.

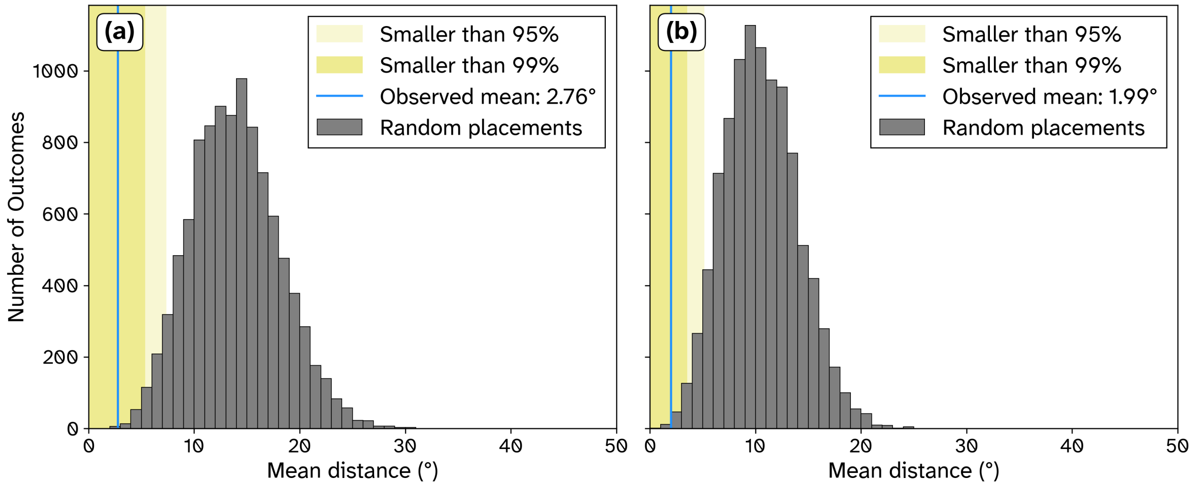

Figure S12. Equivalent of Figure S4b, but using but using LLVP edges defined by the 1% horizontal shear velocity reduction contour at 2800km depth in the tomographic models (a) GLAD-M35 (Cui et al., 2024) and (b) REVEAL (Thrastarson et al., 2024).

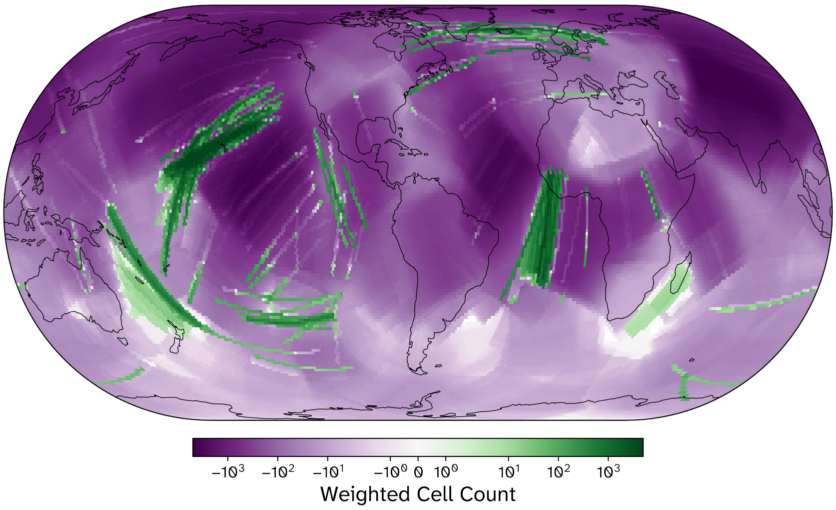

Figure S13. Same as Figure 5 but including the lowest confidence positive picks.

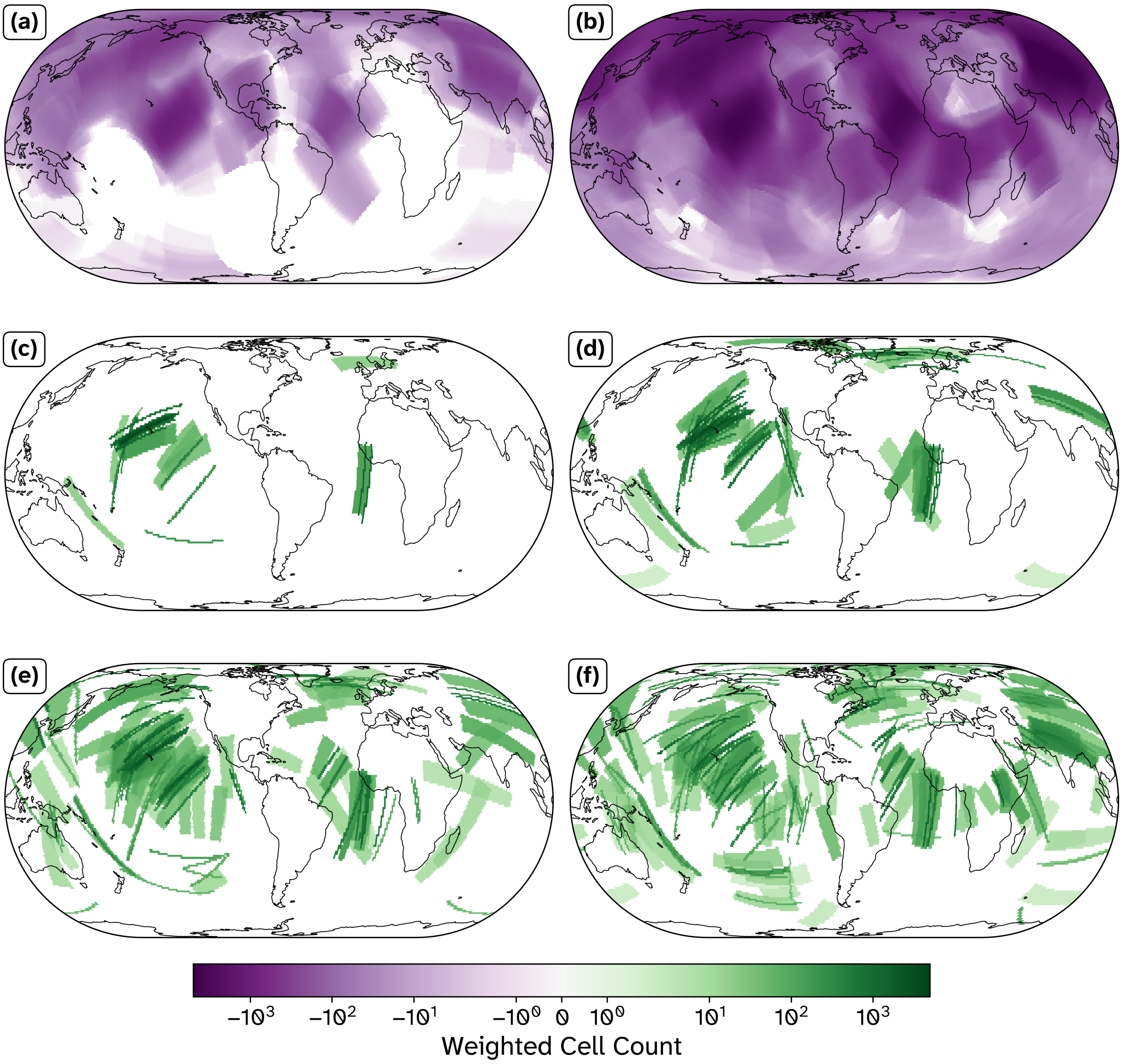

Figure S14. Components of the differential map (Figure S13), split by confidence levels. (a) and (b) show confident and uncertain null detections, while (c)–(f) show positive detections in decreasing order of confidence. Negative detections are given a negative weighting, and positive detections are given a positive weighting.